

## Article

# A New Methodology for Reference Evapotranspiration Prediction and Uncertainty Analysis under Climate Change Conditions Based on Machine Learning, Multi Criteria Decision Making and Monte Carlo Methods

Mojtaba Kadkhodazadeh , Mahdi Valikhan Anaraki, Amirreza Morshed-Bozorgdel  and Saeed Farzin \* 

Department of Water Engineering and Hydraulic Structures, Faculty of Civil Engineering, Semnan University, Semnan 35131-19111, Iran; mkadkhodazadeh@semnan.ac.ir (M.K.); mvalikhan@semnan.ac.ir (M.V.A.); a.morshed@semnan.ac.ir (A.M.-B.)

\* Correspondence: saeed.farzin@semnan.ac.ir

**Abstract:** In the present study, a new methodology for reference evapotranspiration (ET<sub>o</sub>) prediction and uncertainty analysis under climate change and COVID-19 post-pandemic recovery scenarios for the period 2021–2050 at nine stations in the two basins of Lake Urmia and Sefidrood is presented. For this purpose, firstly ET<sub>o</sub> data were estimated using meteorological data and the FAO Penman–Monteith (FAO-56 PM) method. Then, ET<sub>o</sub> modeling by six machine learning techniques including multiple linear regression (MLR), multiple non-linear regression (MNLR), multivariate adaptive regression splines (MARS), model tree M5 (M5), random forest (RF) and least-squares boost (LSBoost) was carried out. The technique for order of preference by similarity to ideal solution (TOPSIS) method was used under seven scenarios to rank models with evaluation and time criteria in the next step. After proving the acceptable performance of the LSBoost model, the downscaling of temperature (T) and precipitation (P) by the delta change factor (CF) method under three models ACCESS-ESM1-5, CanESM5 and MRI-ESM2-0 (scenarios SSP245-cov-fossil (SCF), SSP245-cov-modgreen (SCM) and SSP245-cov-strgreen (SCS)) was performed. The results showed that the monthly changes in the average T increases at all stations for all scenarios. Also, the average monthly change ratio of P increases in most stations and scenarios. In the next step, ET<sub>o</sub> forecasting under climate change for periods (2021–2050) was performed using the best model. Prediction results showed that ET<sub>o</sub> increases in all scenarios and stations in a pessimistic and optimistic state. In addition, the Monte Carlo method (MCM) showed that the lowest uncertainty is related to the Mianeh station in the MRI-ESM2-0 model and SCS scenario.

**Keywords:** reference evapotranspiration; machine learning; TOPSIS; Monte Carlo method; climate change; uncertainty analysis; Lake Urmia; Sefidrood



**Citation:** Kadkhodazadeh, M.; Valikhan Anaraki, M.; Morshed-Bozorgdel, A.; Farzin, S. A New Methodology for Reference Evapotranspiration Prediction and Uncertainty Analysis under Climate Change Conditions Based on Machine Learning, Multi Criteria Decision Making and Monte Carlo Methods. *Sustainability* **2022**, *14*, 2601. <https://doi.org/10.3390/su14052601>

Academic Editor: Marc A. Rosen

Received: 25 October 2021

Accepted: 14 December 2021

Published: 23 February 2022

**Publisher's Note:** MDPI stays neutral with regard to jurisdictional claims in published maps and institutional affiliations.



**Copyright:** © 2022 by the authors. Licensee MDPI, Basel, Switzerland. This article is an open access article distributed under the terms and conditions of the Creative Commons Attribution (CC BY) license (<https://creativecommons.org/licenses/by/4.0/>).

## 1. Introduction

The combined process of water evaporation from the earth's surface and transpiration from vegetation are two important processes integral to the hydrological cycle and have a large share of rainfall losses [1–3]. The most common method of calculating plant evapotranspiration is reference evapotranspiration (ET<sub>o</sub>). In this method, the amount of ET<sub>o</sub> is calculated using meteorological data, and by the single crop coefficient of the desired product, the evapotranspiration of the product can be estimated [4].

Excessive fossil fuels and human interventions have caused global warming. Anthropogenic greenhouse gas emissions were at a record high in the last decade. Recent climate change has impacted human and environmental systems in many ways. Therefore, researchers are looking to prevent global warming and increase ET<sub>o</sub>. For this reason, the quantitative and qualitative protection of water resources is critical [5].

In 2019, due to the Coronavirus disease 2019 (COVID-19) pandemic, extensive restrictions were imposed on travel, industrial and commercial activities by the governments. These restrictions can lead to changes in greenhouse gas emissions on a global scale. Changes in greenhouse gas emissions caused a change in the trend of global warming and consequently changed the trend of precipitation and temperature. Therefore, researchers have estimated greenhouse gas emissions, precipitation and temperature on a global scale considering new scenarios of impacts of post-pandemic of COVID-19 (such as faster growth of green technologies that leads to lower greenhouse gas emissions). Evapotranspiration depends on precipitation and temperature, and changes in these variables can affect evapotranspiration. Hence, the impacts of post-pandemic of COVID-19 may change the predicted evapotranspiration in the future period from those in previous studies [6].

The coupled model intercomparison project (CMIP), established by the world climate research program (WCRP), has committed to producing extensive global climate model (GCM) outputs and has documented some substantial climate change assessment reports (e.g., the fourth and fifth assessment reports of the intergovernmental panel on climate change, IPCC AR4 [7] and AR5 [8]). GCM outputs from several phases of the CMIP have been crucial to climate change research. The most recent CMIP6 phase produced many updated climate model outputs, the majority of which are already accessible and will contribute to the IPCC AR6. In this phase, the combination of using radiative forcing called representative concentration pathways (RCPs) as the basis and considering social and economic factors, together called shared socioeconomic pathways (SSPs), makes future scenarios more reasonable [9]. Based on CMIP6 simulations, some studies have focused on evaluating the ability of CMIP6 climate models to reproduce historical climate variables, climate extremes and ocean-atmosphere systems [10].

A careful estimation of ETo is essential for managing water resources [11,12]. There are several methods for calculating and estimating evapotranspiration. Allen et al. [13] developed a weather data conditioning process to exhibit better the characteristics of the data collected in ETo estimation. Ramírez-Cuesta et al. [14] used an ArcGIS tool called METRIC-GIS for computing crop evapotranspiration. However, the high accuracy and speed of modern methods such as artificial intelligence (AI) have expanded machine learning algorithms in estimating ETo [15].

In recent years, GCMs of AR5 have been used to predict evapotranspiration [16–18]. In another study, Wang et al. [1] investigated the uncertainty of the CMIP6 model by using the signal-to-noise ratio (SNR) to evaluate the global terrestrial ET.

Recently, hybrid machine learning algorithms have gained popularity in the modeling ETo [19–22]. In addition, artificial neural network (ANN), adaptive fuzzy neural inference system (ANFIS), support vector machine (SVM), MARS, gene expression programming (GEP) and RF models have been used to predict ETo [23–28]. Wu et al. [29] used different machine learning methods for predicting daily ETo. The results showed that the SVM model had better performance than the other models. Walls et al. [30] used different ANN structures for modeling the ETo and reported that the ANN model has good accuracy for predicting ETo. Kaya et al. [31] modeled ETo using multilayer perceptron, support vector regression and multilinear regression models. The results showed that the multilayer perceptron model performs better than the other algorithms. Bellido-Jimenez et al. [32] employed different machine learning methods such as multilayer perceptron and extreme learning machine for modeling ETo with results that indicated their good application. Mohammadrezapour et al. [33] applied SVM, ANFIS and GEP models to estimate potential ETo. Findings showed that the SVM model performed better than the other models. Zhu et al. [34] and Tikhamarine et al. [35] used a new hybrid AI model for modeling ETo. The results showed that the new hybrid AI model had better performance than the other models.

The purpose of this paper is to predict and analyze ETo uncertainty under the conditions of climate change and the effects of the COVID-19 post-pandemic recovery. As far as we know, there are no reports of simultaneous use of machine learning, TOPSIS

method, Delta CF method and MCM method for ETo prediction and uncertainty analysis influenced by climate change and COVID-19. Therefore, in the present study, first, the ETo will be modeled by using six powerful machine learning methods, including MLR, MNLR, MARS, M5, RF and LSBoost (in the nine different stations at the Lake Urmia and Sefidrood basins). Afterward, the best machine learning will be selected by TOPSIS and accuracy and time computation criteria will be considered. Then, T and P will be downscaled by delta CF method and outputs of the three CMIP6-GCMs (ACCESS-ESM1-5, CanESM5 and MRI-ESM2-0) and three scenarios (SSP245-cov-fossil, SSP245-cov-modgreen and SSP245-cov-strgreen). In the next stage, the ETo will be predicted by using downscaled T and P data and the best-selected machine learning. Finally, uncertainty analysis will be performed, and GCMs and scenarios with the least and most uncertainty will be reported. Therefore, in this study, using these methods, a new methodology is proposed for a more accurate analysis of ETo on the future horizon. This methodology has a high potential for analyzing and predicting other hydrological and water resources parameters under climate change and the COVID-19 post-pandemic recovery.

## 2. Materials and Methods

### 2.1. Present Work Steps

Figure 1 shows the general framework and details of the new methodology for predicting and analyzing ETo uncertainty. The limitations of this method are as follows:

1. Adequate and reliable data is required.
2. Machine learning requires preprocessing of input data to achieve accurate results.
3. The Monte Carlo method requires probabilistic distribution functions to generate input data.

The work steps are as follows:

Step 1: Estimation of ETo

- ETo data are estimated by FAO-56 PM method based on meteorological data (minimum T (min-T), maximum T (max-T), solar radiation, humidity, wind speed and sunny hours) at the different stations.
- The data is divided into training (70%) and testing (30%) periods.

Step 2: Modeling ETo and selecting the best model

- Six machine learning algorithms, including MLR, MNLR, MARS, M5, RF and LSBoost are employed for estimating CIP removal value.
- Because in modeling ETo and comparing algorithms, various factors such as evaluation criteria and calculation time affect selecting the best model, the TOPSIS method is used to select the best algorithm. This process is as follows:
  1. Evaluation criteria, including MAE, RMSE, R, MARE, RRMSE and the run times of algorithms, are considered as criteria of the TOPSIS method.
  2. Algorithms including MLR, MNLR, MARS, M5, RF and LSBoost are considered as alternatives.
  3. The TOPSIS method is used under seven scenarios to select the best algorithm. The lambda time weight varies from 0.091 to 0, and the lambda weight of the other criteria is the same in all scenarios.
  4. In the last step in each scenario, the algorithm with the highest score is selected as the best algorithm. Figure A1 (Appendix A.1) shows the TOPSIS structure for selecting the best algorithm.

Step 3: Downscaling

- At this step, the delta CF method is used to downscale T and P using three models (ACCESS-ESM1-5, CanESM5 and MRI-ESM2-0) and three scenarios (SCF, SCM and SCS) were used.

Step 4: Prediction ETo by the best model (2021–2050)

- ETo prediction for the period 2021–2050 under the influence of climate change is performed by downscaled T and P data and the best algorithm in nine stations.

Step 5: Uncertainty analysis

- Uncertainty analysis of models and scenarios is performed using the MCM in different stations.

**A new methodology for reference evapotranspiration prediction and uncertainty analysis under climate change conditions based on machine learning, multi criteria decision making and Monte Carlo methods** (Kadkhodazadeh et al., 2021 ).

- Case study: Urmia lake basin and Sefidrood basin
- Stations under study: Tabriz, Sahand, Urmia, Maragheh, Mianch, Mahabad, Saqez, Takab, Zanjan

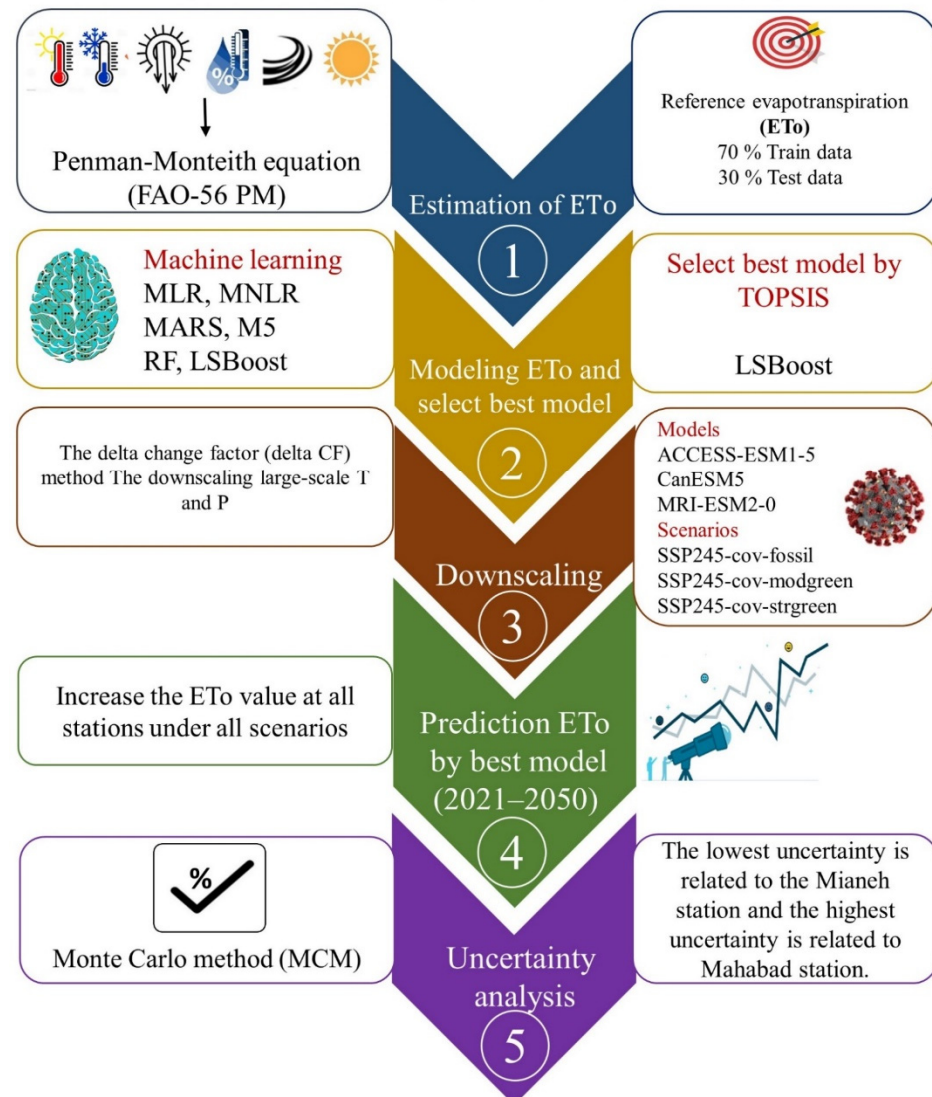


**Figure 1.** Framework for ETo prediction and assessment of its uncertainty.

## 2.2. Penman-Monteith Equation (FAO-56 PM)

In recent years, instead of using ETo data measured at meteorological stations [24], the FAO-56 PM method has been used to estimate ETo [36,37]. The present study implemented the FAO-56 PM method to estimate the ETo from meteorological data. This equation is renowned as the standard and popular model for estimating ETo across the world, presented by the international commission for irrigation and drainage (ICID) and FAO [4]. In this method, the amount of evapotranspiration is estimated for a hypothetical grass reference crop with an assumed crop height of 0.12 m, a fixed surface resistance of  $70 \text{ sm}^{-1}$

and an albedo of 0.23. Evapotranspiration of other plants can be measured using ETo and the single crop coefficient. The FAO-56 PM method is given in Appendix A.2.

### 2.3. Multiple Linear Regression (MLR)

MLR is commonly used to estimate the linear regression relationship between inputs and target values using severe data deviations [38,39]. There is a dependent variable and two or more independent variables in this model. One of the advantages of this model is that it can minimize changes due to ambiguities. In MLR, the relationship between inputs and goals is assumed to be as follows:

$$Y = B_0 + B_1X_1 + B_2X_2 + \dots + B_nX_n + \varepsilon \quad (1)$$

where  $B_0$  refers to Y-intercept, where as  $X_1, X_2 \dots X_n$  stands for the independent variables and  $B_1, B_2 \dots B_n$  are the coefficients of independent variables,  $\varepsilon$  refers to the error term and Y is the dependent variable.

### 2.4. Multiple Non-Linear Regression (MNLr)

The basis of this model is to create a nonlinear relationship between input and output variables. The MNLr model, unlike the MLR model, establishes a nonlinear relationship between dependent and independent variables [40]. The relationship between inputs and targets values in MNLr is as follows:

$$Y = B_0 + B_1X_1 + B_2X_2 + \dots + B_nX_n + B_{n+1}X_1^2 + B_{n+2}X_2^2 + \dots + B_{2n}X_n^2 + \varepsilon \quad (2)$$

### 2.5. Multivariate Adaptive Regression Splines (MARS)

The MARS model is a non-parametric regression approach introduced by Friedman [41]. The MARS model has good potential for solving nonlinear problems with high dimensions. The MARS model couples recursive segmentation and spline fitting by dividing the overall data into several subsets [42]. This algorithm searches for a nonlinear relationship in an extensive data set to create an acceptable model by determining the weights of input variables regarding the corresponding target. The MARS algorithm produces basis functions for input variables and then determines regression models by combining basis functions to estimate the output variable [43].

MARS uses the following basis function to confirm the input/output relationship between the nodes [44].

$$hm(x) = \max(0, c - x) \text{ or } \max(x - c, 0) \quad (3)$$

where x is an input variable, c is a threshold value for input variable x and  $hm(x)$  is the basis function. MARS common model is introduced as follows:

$$Y = \beta_0 + \sum_{i=1}^M \beta_m hm(x) \quad (4)$$

where Y is an output variable,  $\beta_0$  is a constant value, M is several functions and  $\beta_m$  is a corresponding coefficient of  $hm(x)$ .

### 2.6. M5 Model Tree (M5)

The M5 algorithm was initially improved by Quinlan [45]. The M5 algorithm is a data mining technique that has two phases:

- Dividing the inputs area into several subsets and using a linear regression model according to partial attribute values for each subset.
- In each node, a linear regression is established.

The M5 algorithm structure is like a tree grown from the root (first node) to the leaves. The branches consist of a number range from the primary node to the descendant node [46]. The criteria for growing the M5 algorithm is standard deviation reduction (SDR) [47]:

$$\text{SDR} = \text{SD}(T) - \sum_i \frac{|T_i|}{|T|} \text{SD}(T_i) \quad (5)$$

where  $T$  is a subset of data at each node,  $T_i$  is the set of attribute values obtained by dividing  $T$  and  $\text{SD}$  is the standard deviation. More details regarding how the M5 algorithm is running can be found in Wang and Witten [48]. Figure A2 (Appendix A.3) shows the structure of the M5 model.

### 2.7. Random Forest (RF)

The random forest is a famous machine learning program for solving regression difficulties in different engineering fields, such as estimating the sea surface salinity, nanofluids, groundwater pollution, etc. [49,50]. This program attempts to obtain non-linear relationships between inputs and outputs by incorporating the M5 model tree and bagging to improve the performances of standalone M5. The ensemble method developed itself by making independent M5 model trees and decreasing errors generated from limited and unstable regression. The random forest produces several M5 model trees using two preceding randomization operators: In the first operator, a subset  $\theta$  is provided randomly from train data for each independent M5 model tree. The mathematical explanation of this operator is defined as follows:

$$S = \{T(x, \theta_1), T(x, \theta_2), \dots, T(x, \theta_n)\} \quad (6)$$

where  $S$ ,  $T$ ,  $x$ , and  $\theta$  are the sets of the M5 model tree results, M5 model tree, train data and randomized subset, respectively.

This operator is an iterative method in leaf nodes; however,  $T(x, \theta_n)$  is replaced through a weighted average of the trained values. The weighted average is measured as follows:

$$w_i(x, \theta) = \frac{x_i}{\sum x_i}, \quad i = 1, 2, \dots, n, \quad \sum w_i = 1 \quad (7)$$

The different and randomized input variables subset is utilized at all nodes of M5 model tree within the second operator [51]. Each input variable subset is related to training data,  $Y_i$ , is classified in each single decision tree, and hence, the ultimate evaluation of RF is determined as the following equation:

$$O_x = \sum_{i=1}^n \frac{1}{n} w_i(x, \theta) Y_i \quad (8)$$

where  $O_x$ ,  $n$  represent the output of train data and number of single trees.

Figure A3 (Appendix A.4) shows the structure of the RF model.

### 2.8. Least-Squares Boost (LSBoost)

Ensemble learning methods (or ensembles or majority voting models) are among the most popular devices to increase accuracy and reliability and reduce the bias and variance of results than standalone learner instances [52]. The most common ensemble approaches are bagging (parallel) and boosting (sequential).

Friedman [53] developed LSBoost based on the least square, absolute and Huber loss function. Among all ensemble approaches in regression problems, the LSBoost algorithm is a state-of-the-art gradient boosting algorithm. LSBoost first trains a start by training the individual weak learners such as decision tree, and during iterative process fits the residual

of errors to establish a better relationship between inputs and targets. LSBoost uses the following equation to estimate target values:

$$F_M(\vec{x}) = F_0(\vec{x}) + v^* \sum_{i=1}^M \alpha_m B_m(\vec{x}) \quad (9)$$

where  $F_0(\vec{x})$  is aggregated prediction for input values  $(\vec{x})$ ,  $B_1 \dots B_M$  are standalone weak learners,  $\alpha_1 \dots \alpha_M$  are weights of weak learner and  $v^*$  is learning ratio.

### 2.9. Technique for Order of Preference by Similarity to Ideal Solution (TOPSIS)

Yoon [54] introduced the TOPSIS method for multi criteria decision making. In this method, the best alternative is closest to the positive ideal solution (PIS) and far from the negative ideal solution (NIS). See Appendix A.5 for more details.

In the TOPSIS method, an alternative with more scores is a better alternative. The TOPSIS method is easy to use and has a more straightforward structure than other multi criteria decision making methods.

### 2.10. Delta Change Factor (CF) Method for Downscaling CMIP6 GCMs Data

The delta CF method is a widely utilized downscaling approach frequently used to downscale GCM outputs [55]. The CF approach is used to calculate long-term monthly averages of temperature and rainfall. Equations (10) and (11) are used to downscale the amount of long-term average temperature change and the long-term average rainfall change ratio for each month for the next thirty years (2021–2050). These computations are carried out for each scenario based on each GCM.

$$\Delta T_{i,j} = \left( \bar{T}_{GCMfu_{i,j}} - \bar{T}_{GCMbas_{i,j}} \right) \quad (10)$$

$$\Delta P_{i,j} = \left( \frac{\bar{P}_{GCMfu_{i,j}}}{\bar{P}_{GCMbas_{i,j}}} \right) \quad (11)$$

The scenario-based monthly average P change ratio and monthly average T change associated with the  $i$ th model in the  $j$ th month are represented by  $\Delta T_{i,j}$  and  $\Delta P_{i,j}$ , respectively. The  $i$ th model's simulated long-term average T and P in the  $j$ th month for the future period is  $\bar{T}_{GCMfu_{i,j}}$  and  $\bar{P}_{GCMfu_{i,j}}$ , and the  $i$ th model's simulated long-term average T and P in the  $j$ th month of the base period is  $\bar{T}_{GCMfu_{i,j}}$  and  $\bar{P}_{GCMfu_{i,j}}$ . Using Equations (12) and (13), the values of T and P variables in different future periods are calculated by incorporating the corresponding change values into the observed data in the base period:

$$T_{i,K} = T_{obs,K} + \Delta T_{i,j} \quad (12)$$

$$P_{i,K} = P_{obs,K} + \Delta P_{i,j} \quad (13)$$

where  $T_{i,K}$  and  $P_{i,K}$  represent the predicted temperature and precipitation for the  $i$ th model in the  $k$ th time step (sequential month) in the future period, and  $T_{obs,K}$  and  $P_{obs,K}$  are the temperature and precipitation of the  $k$ th time step within the historical period, respectively [56,57].

### 2.11. Monte Carlo Method (MCM)

Although there are several factors in ETo forecast uncertainty, this study focuses on uncertainties related to forecasting scenarios and models [58]. Stochastic data are generated using the Monte Carlo simulation method [59]. According to Figure A4 (Appendix A.6.), the steps of this method are as follows:

- Each input data is assigned an appropriate distribution function.
- Using the selected distribution functions, 1000 new data time series are generated for each input.

- The output corresponding to each data time series generated by the distribution functions is predicted.
- Predicting new outputs, a 95% prediction confidence interval is obtained using the values generated for each observation to quantify the prediction uncertainties.
- Sort upper and lower band of 95% confidence interval for each time series.
- The upper quartile (97.5%) and the lower quartile (2.5%) of the 95% band are determined.
- The R-factor coefficient is calculated using the following formula. The lower the value of this coefficient, the less uncertainty.

$$R\text{-factor} = \frac{S_p}{S_x} \quad (14)$$

$$S_p = \sum_{i=1}^N (U_L^i - L_L^i) / N \quad (15)$$

where  $S_x$  is the standard deviation of the observed values,  $N$  is the number of observed data and  $U_L^i$  and  $L_L^i$  indicate the  $i$ th value of the upper quartile (97.5%) and the lower quartile (2.5%) of the 95% band.

### 2.12. Evaluation of Model Performance

In the present study, various evaluation criteria, including mean absolute error (MAE), root mean square error (RMSE), person correlation coefficient (R), mean absolute relative error (MARE) and relative root mean square error (RRMSE) are employed for evaluation of machine learning algorithms. The mentioned evaluation criteria are given in Appendix A.7 [60–62].

### 2.13. Study Area and Data Materials

The nine stations, including Tabriz, Sahand, Urmia, Maragheh, Mianeh, Mahabad, Saqez in the Lake Urmia basin, Takab and Zanjan in the Sefidrood basin, were selected to investigate the application of machine learning in estimating and predicting ETo. The Urmia Lake basin is one of the important basins of Iran because the largest Lake of Iran (Urmia Lake) is located in this basin [63]. The Urmia basin area is about 51,460 km<sup>2</sup>. The other considered basin in this study is the Sefidrood basin. The importance of this basin is for the perennial river of Sefidrood, which drains a 59,217 km<sup>2</sup> area. The climates of these sites are cold and dry, and the ETo rate is low. Figure 2 shows the location of employed stations in the Urmia basin, Sefidrood basin and Iran.

This study considers the min-T, mean-T, max-T, humidity, wind speed and P as inputs for modeling ETo. Table A1 (Appendix A.8) shows the mean and standard deviation (Std) of inputs and target values for nine investigated stations.

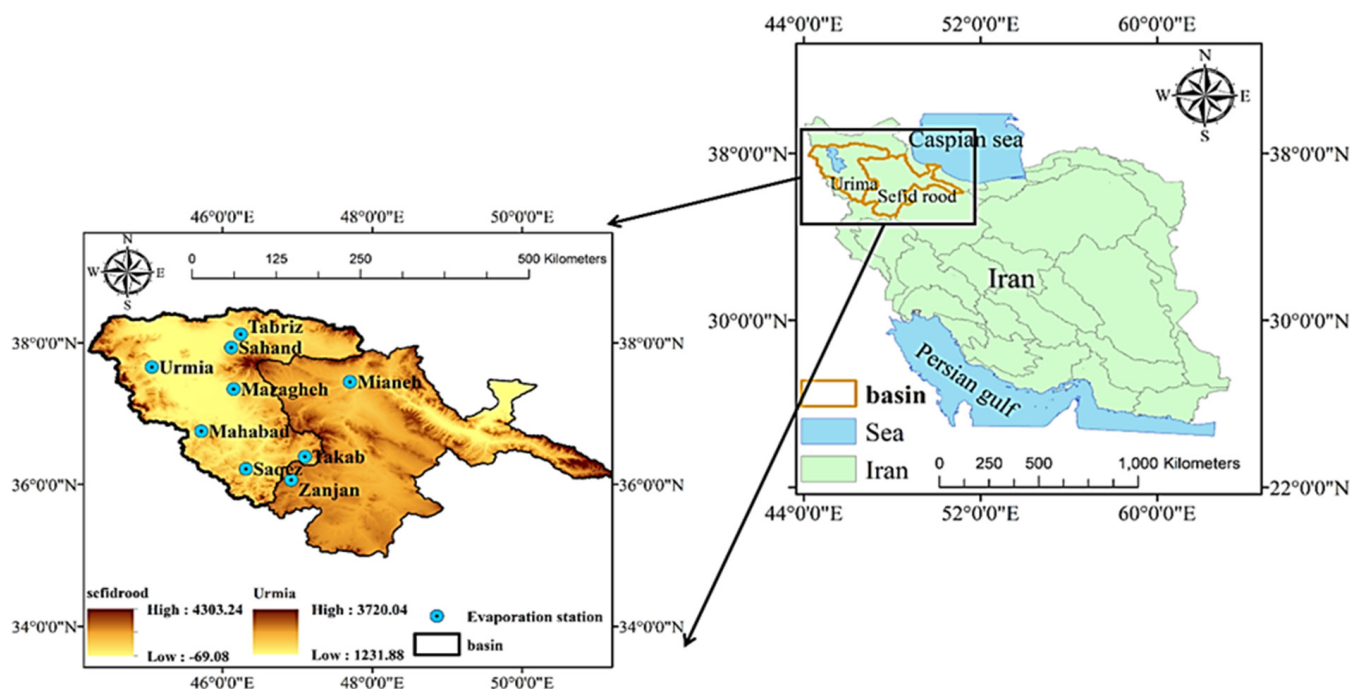


Figure 2. Case study locations.

2.14. GCMs and Future Climate Change Scenarios

For this study, we used three COVID-19 affected pathways (SSP245-cov-fossil, SSP245-cov-modgreen and SSP245-cov-strgreen) from CMIP6, which assume a moderate growth route in which future socioeconomic development patterns follow existing development tendencies, resulting in a forcing pathway of 4.5 Wm<sup>-2</sup> in 2100 and the effects of population changes, economic growth, urbanization and [64,65] COVID-19.

Furthermore, research has demonstrated that the impact of COVID-19 related changes in human activity can be seen in atmospheric composition [66], particularly in the amount of solar radiation reaching the planet’s surface and aerosol optical depth across southern and eastern Asia. Using three GCM outputs (ACCESS-ESM1-5, CanESM5 and MRI-ESM2-0) and three SSP-RCP scenarios from the most recent CMIP6, we looked at ETo for historical and future periods. Essential model outputs for the historical period (1985–2014) and future period (2021–2050) were downloaded for this study, including monthly P, max-T, min-T, wind speed, downward shortwave radiation and relative humidity [67]. Selected scenarios are based on current and future global climate impacts resulting from COVID-19 [64], the climate Response to Emissions Reductions [6] and modifying emissions scenario projections to account for the effects of COVID-19 [65]. Three assumptions were used for COVID-19 post-pandemic recovery scenarios with the SSP245 scenario as the baseline. The details of the selected models and scenarios are presented in Tables 1 and 2 and Appendix A.9 [64,65,68–72].

Table 1. The considered CMIP6 GCMs.

Centre	Model	Atmosphere Resolution <sup>a</sup>
Commonwealth Scientific and Industrial research Organization (Australia)	ACCESS-ESM1-5	250 km (N96), L38
Canadian Center for Climate Modelling and Analysis (Canada)	CanESM5	500 km (T63), L49
Meteorological Research Institute (Japan)	MRI-ESM2-0	100 km (TL159, 1.125°), L80

<sup>a</sup> shown as CMIP “nominal resolution” in km, “L” indicates number of vertical levels.

**Table 2.** SSP scenarios.

Experiment-Id	Activity-Id	Description
SSP245-cov-fossil (SCF)	DAMIP	Future scenario based on SSP245, but following a path of increased emissions due to a fossil-fuel rebound economic recovery from the COVID-19 pandemic restrictions. Concentration-driven
SSP245-cov-modgreen (SCM)	DAMIP	Future scenario based on SSP245, but following a path of reduced emissions due to a moderate-green stimulus economic recovery from the COVID-19 pandemic restrictions. Concentration-driven
SSP245-cov-strgreen (SCS)	DAMIP	Future scenario based on SSP245, but following a path of reduced emissions due to a strong-green stimulus economic recovery from the COVID-19 pandemic restrictions. Concentration-driven

### 3. Results and Discussion

#### 3.1. ETo Modeling by Machine Learning

Table 3 shows the performance of all applied models during the training and testing periods for estimation of ETo at four important stations. In Tabriz station, the LSBoost model showed the best predictive capabilities. Based on the results obtained, LSBoost was characterized by the highest value of R and the lowest error values (MAE = 0.15, RMSE = 0.05, MARE = 0.11, RRMSE = 0.03). The modeling results in the Urmia station showed that the RF model has the highest accuracy. Values of MAE, RMSE, R, MARE and RRMSE were 0.14, 0.04, 0.99, 0.10 and 0.03, respectively. In the Mahabad station, the M5 model provided good results too. The lowest values of MAE, RMSE, MARE and RRMSE were equal to 0.17, 0.05, 0.11, 0.04, respectively, and the highest value of R was equal to 0.99. The modeling results of other stations are stated in Appendix B.1 and Table A2.

**Table 3.** Results of the algorithms to the ETo modeling at the different stations.

	Train					Test				
	Tabriz									
	MAE	RMSE	R	MARE	RRMSE	MAE	RMSE	R	MARE	RRMSE
MLR	0.27	0.12	0.97	0.22	0.08	0.32	0.16	0.97	0.29	0.10
MNLR	0.20	0.07	0.98	0.14	0.05	0.23	0.08	0.99	0.16	0.05
MARS	0.14	0.04	0.99	0.11	0.02	0.17	0.05	0.99	0.12	0.03
M5	0.10	0.03	0.99	0.07	0.02	0.17	0.07	0.99	0.12	0.04
RF	0.09	0.02	1.00	0.06	0.01	0.16	0.05	0.99	0.11	0.04
LSBoost	0.05	0.00	1.00	0.04	0.00	0.15	0.05	0.99	0.11	0.03
	Urmia									
	MAE	RMSE	R	MARE	RRMSE	MAE	RMSE	R	MARE	RRMSE
MLR	0.26	0.10	0.97	0.20	0.07	0.54	1.07	0.79	0.33	0.70
MNLR	0.19	0.06	0.99	0.12	0.04	0.51	1.04	0.80	0.27	0.68
MARS	0.17	0.05	0.99	0.11	0.03	0.21	0.07	0.99	0.14	0.04
M5	0.05	0.01	1.00	0.03	0.01	0.16	0.08	0.98	0.10	0.05
RF	0.11	0.02	0.99	0.06	0.02	0.14	0.04	0.99	0.10	0.03
LSBoost	0.00	0.00	1.00	0.00	0.00	0.15	0.04	0.99	0.10	0.03

Table 3. Cont.

	Train						Test			
	Mahabad									
MLR	0.27	0.11	0.98	0.19	0.08	0.54	1.08	0.78	0.31	0.73
MNLR	0.23	0.08	0.98	0.14	0.06	0.52	1.04	0.79	0.27	0.70
MARS	0.23	0.09	0.98	0.13	0.06	0.23	0.08	0.98	0.15	0.05
M5	0.15	0.04	0.98	0.08	0.03	0.17	0.05	0.99	0.11	0.04
RF	0.13	0.04	0.98	0.07	0.03	0.24	0.13	0.97	0.15	0.09
LSBoost	0.00	0.00	0.98	0.00	0.00	0.18	0.06	0.99	0.11	0.04

Figures 3 and A5 (Appendix B.2) show the violin plot of monthly ETo estimated by different models at the nine stations. As seen, for modeled ETo by investigated algorithms like observed ETo, the most and least amounts of ETo have more probability than middle amounts of ETo. Besides, in almost all stations, the median and quartile of modeled ETo by MARS, M5, RF and LSBoost were closer to the median and quartile of the observed data. According to Figures 3 and A5, the average of the data estimated by the models was close to the observation data, which shows the better performance of the models. In Takab station the MARS model had the best performance among other models. The M5 model in Mahabad station showed better performance than other algorithms in estimating values and, in most cases, the difference between the estimated values and the observed values was very small. In Sahand, Urmia and Zanjan stations, the RF model had the highest accuracy. In Tabriz, Maragheh, Mianeh and Saqez stations, the LSBoost model had the best performance.

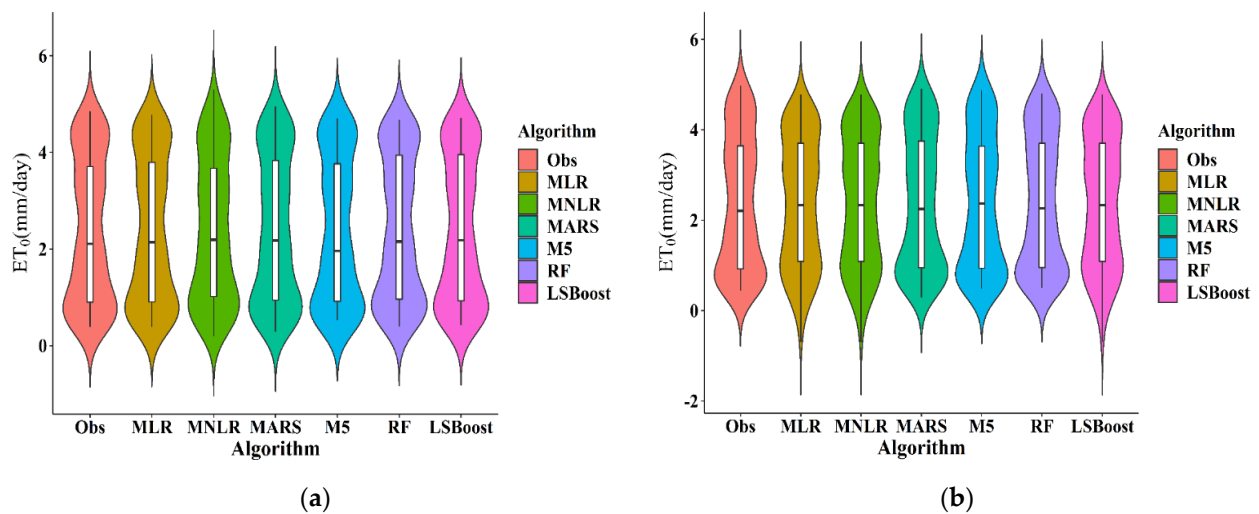
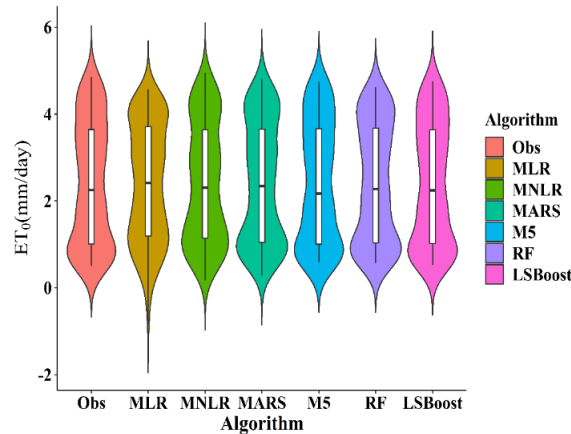


Figure 3. Cont.



(c)

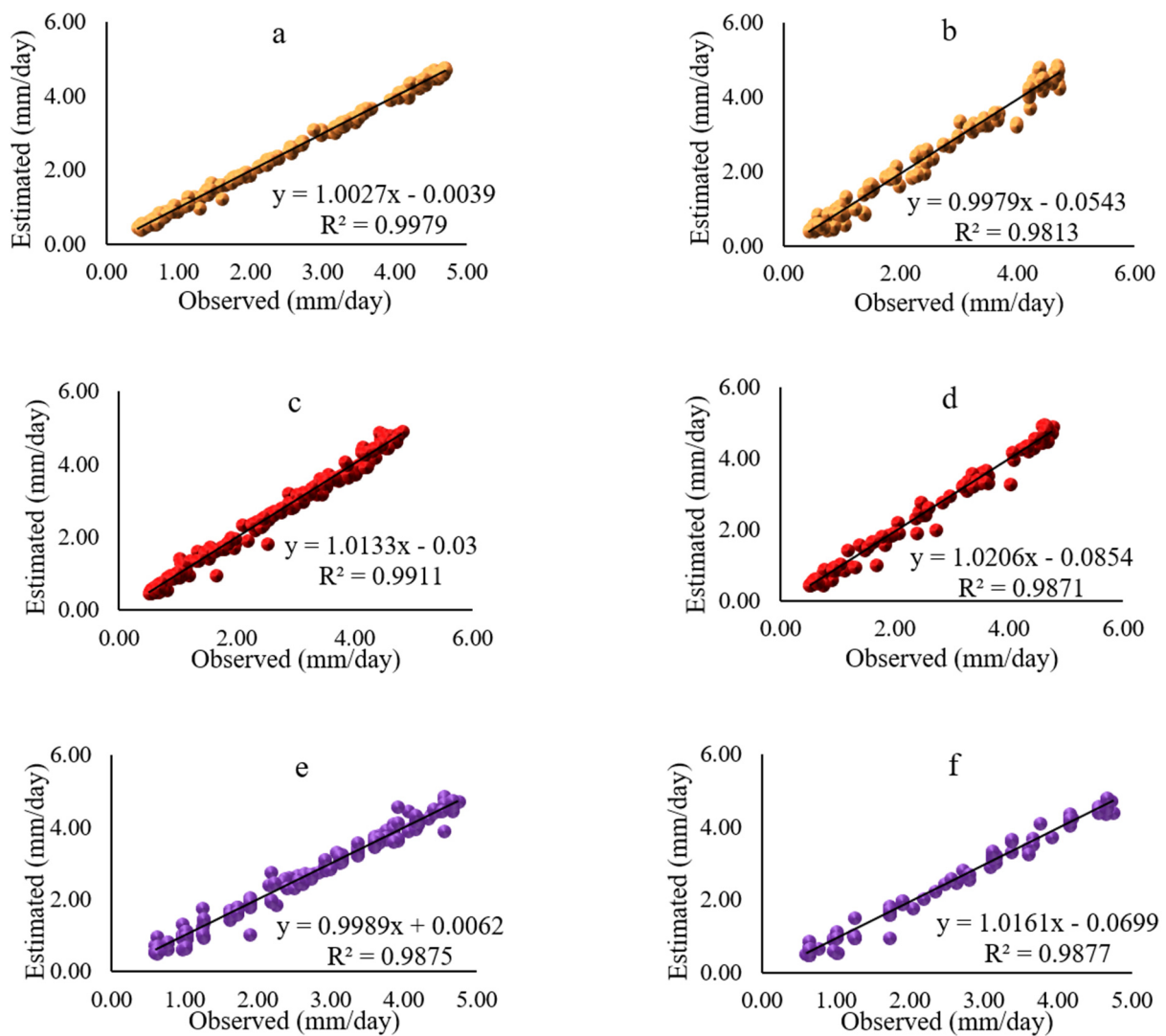
**Figure 3.** Violin plot of daily mean ETo estimated by different models. (a) Tabriz, (b) Urmia, (c) Mahabad.

Table 4 shows the mean values of the evaluation criteria at different stations by MLR, MNLR, MARS, M5, RF and LSBoost algorithms and the run time of different algorithms. However, it is impossible to say which model performs better due to the difference in criteria and the results obtained at different stations. Therefore, the TOPSIS method is used for selecting the best algorithm.

**Table 4.** Mean results in the testing period and run time of algorithms.

	MAE	RMSE	R	MARE	RRMSE	Time(s)
MLR	0.41	0.56	0.89	0.28	0.37	0.41
MNLR	0.35	0.51	0.90	0.21	0.34	1.07
MARS	0.21	0.06	0.99	0.14	0.04	1.46
M5	0.19	0.09	0.98	0.12	0.06	0.14
RF	0.18	0.06	0.99	0.12	0.04	5.73
LSBoost	0.18	0.06	0.99	0.11	0.04	1.11

Figures 4 and A6 (Appendix B.3) show the scatter plots in the training and testing periods by the best algorithms in the nine stations. According to Figures 4 and A6, the difference between the estimated values by the best models and the observed values was very small. The high value of the correlation coefficient means the proper performance of the models is in the modeling of ETo. Since most of the values have accumulated around the semiconductor line, the accuracy of the algorithms was high.



**Figure 4.** The results of the scatter plots by the best algorithm. (a) Tabriz-train, (b) Tabriz-test, (c) Urmia-train, (d) Urmia-test, (e) Mahabad-train, (f) Mahabad-test.

### 3.2. Selecting the Best Machine Learning

In the TOPSIS method, five scenarios were defined in Table 5. In scenario 1, the weight of all criteria is the same, and the lambda weight of time decreases with increasing the ID of the scenario. Based on Table 5, the lambda weight of time varied from 0.091 to 0. In addition, the lambda weight of other assessment criteria was considered equal, and the sum of all assessment criteria needed to be equal to one. The lambda weight of other criteria was varied from 0.200 to 0.182. The scores of algorithms from the TOPSIS method were listed in Table 6. The algorithms with the maximum score have a better rank. The results showed LSBoost has more scores in most of the scenarios. The LSBoost model with fast convergence improved modeling accuracy because it is an ensemble method and uses different weight sequences of different distribution algorithms. This model also produces very powerful regression techniques. Furthermore, the average scores of all scenarios showed that LSBoost had the first rank, and M5, MARS, RF, MNLR and MLR were ranked next, respectively.

**Table 5.** Lambda weight in different scenarios for TOPSIS method.

	MAE	RMSE	R	MARE	RRMSE	Time(s)
Scenario1	0.182	0.182	0.182	0.182	0.182	0.091
Scenario2	0.195	0.195	0.195	0.195	0.195	0.024
Scenario3	0.198	0.198	0.198	0.198	0.198	0.010
Scenario4	0.199	0.199	0.199	0.199	0.199	0.005
Scenario5	0.199	0.199	0.199	0.199	0.199	0.003
Scenario6	0.200	0.200	0.200	0.200	0.200	0.002
Scenario7	0.200	0.200	0.200	0.200	0.200	0.000

**Table 6.** Scores of TOPSIS for ranking of algorithms.

	MLR	MNLR	MARS	LSBoost	M5	RF
Scenario1	0.79	0.70	0.76	0.83	0.99	0.20
Scenario2	0.48	0.45	0.83	0.88	0.96	0.51
Scenario3	0.27	0.28	0.90	0.94	0.94	0.71
Scenario4	0.16	0.20	0.92	0.97	0.94	0.83
Scenario5	0.10	0.18	0.93	0.98	0.94	0.89
Scenario6	0.07	0.17	0.94	0.99	0.94	0.93
Scenario7	0.00	0.16	0.94	1.00	0.94	0.99
Average	0.18	0.24	0.91	0.96	0.94	0.81
Rank	6	5	3	1	2	4

Figures 5 and A7 (Appendix B.4) show the histogram of the error in modeling ETo by the best algorithm (LSBoost) at different stations. The frequency value indicates the number of items in each error interval in histograms. The accuracy of the modeling depends on the frequency value in the zero range. In all stations, the frequency value in the error range equal to zero showed that the evaluation criteria obtained from modeling with the LSBoost algorithm were in a very good range and the observed and modeled values of ETo very close.

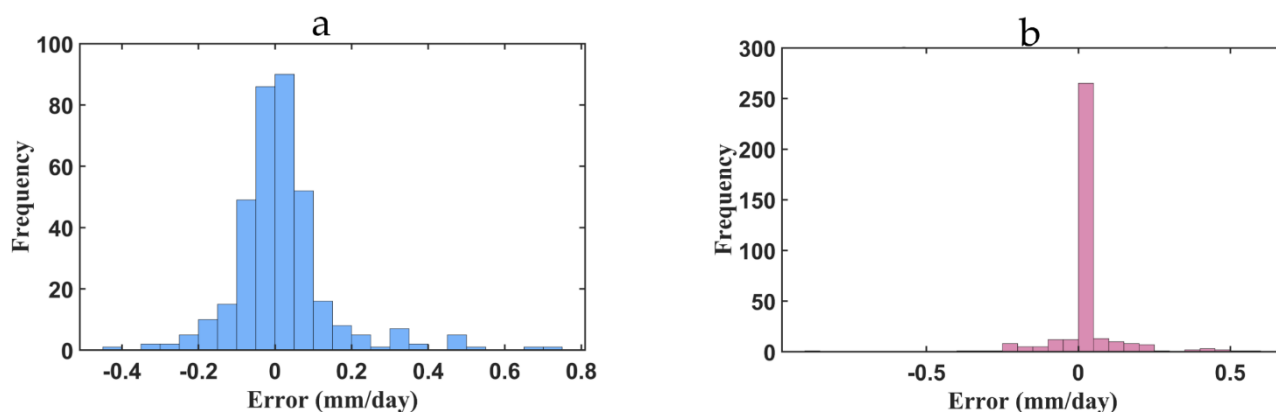


**Figure 5.** Cont.

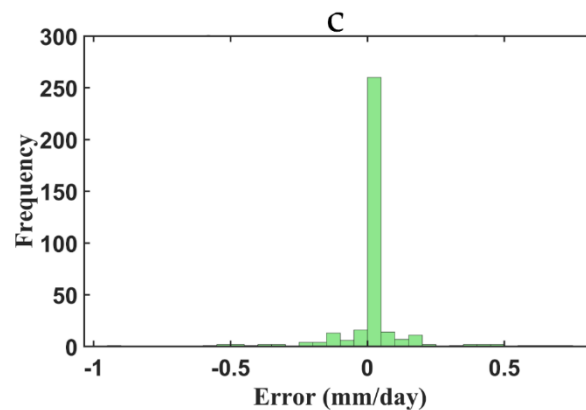


**Figure 5.** The histogram of the error in modeling ETo by the best algorithm. (a) Tabriz, (b) Urmia, (c) Mahabad.

### 3.3. Downscaling T and P

T and P have a large effect on the amount of ETo in the study basin. Large-scale GCMs predict T and P. Therefore, in this study, using the delta CF method, the downscaling of the T scale and P has been done to investigate the effect of climate change on ETo.

According to Tables 7 and A3 (Appendix B.5), The effect of climate change on T and P at the nine stations was investigated, using the comparison of values predicted in the period 2021–2050 with those in the observation. As shown in Figure A8 (Appendix B.6), in terms of the T, the Zanjan station under the CanESM5 model and SCF scenario had the highest change (0.83 °C). The Saqez, Takab and Zanjan stations under the ACCESS-ESM1-5 model and SCM scenario had the lowest change (0.32 °C). Compared to the historical period (11.20 mm/day), the highest increase in P in the future was related to the Mianeh station in the CanESM5 model and the SCS scenario. In Saqez station, the amount of P in the MRI-ESM2-0 model and SCS scenario had the highest decrease (−1.43 mm/day). As seen, the monthly average T change in all stations for all scenarios and future periods increased. The monthly average P change ratio increased in most stations, models and scenarios.

**Table 7.** Downscaling of T and P at the different stations.

Station	Model-Scenario	$\Delta T$ (°C)	$\Delta P$ (mm/Day)	Station	Model-Scenario	$\Delta T$ (°C)	$\Delta P$ (mm/Day)
Tabriz	A-SCF	0.53	2.20	Mahabad	A-SCF	0.56	3.36
	A-SCM	0.34	1.54		A-SCM	0.36	2.69
	A-SCS	0.45	1.43		A-SCS	0.46	3.05
	C-SCF	0.69	2.49		C-SCF	0.69	4.28
	C-SCM	0.55	2.15		C-SCM	0.55	2.49
	C-SCS	0.53	2.09		C-SCS	0.53	3.77
	M-SCF	0.61	−0.16		M-SCF	0.60	−0.65
	M-SCM	0.45	1.44		M-SCM	0.44	2.59
	M-SCS	0.42	0.20		M-SCS	0.41	−1.13
Urmia	A-SCF	0.59	2.64				
	A-SCM	0.39	2.14				
	A-SCS	0.50	2.47				
	C-SCF	0.69	2.64				
	C-SCM	0.55	2.37				
	C-SCS	0.53	3.11				
	M-SCF	0.59	0.46				
	M-SCM	0.43	2.26				
M-SCS	0.39	−0.28					

### 3.4. Prediction of ETo

After the downscaling of the T and P, the prediction of ETo changes in future periods by the best algorithm has been performed under three models: ACCESS-ESM1-5, CanESM5 and MRI-ESM2-0, and three scenarios: SCF, SCM and SCS. The mean, minimum and maximum predicted values in all stations were calculated using the mentioned models and scenarios. According to Tables 8 and A4 (Appendix B.7), comparing the predictions made in different scenarios at Tabriz station, the highest amount of ETo changes (2.91%) were related to the ACCESS-ESM1-5 model and SCF scenario. The lowest ETo changes (1.43%) were related to the MRI-ESM2-0 and SCS scenario. In the Sahand station, the largest changes (3.28%) were predicted by the ACCESS-ESM1-5 model and SCF scenario. However, the least ETo changes (1.83%) were related to the ACCESS-ESM1-5 model and SCM scenario. In Urmia and Maragheh stations, the highest rate of ETo changes was predicted to be 3.84% and 2.28%, respectively, by the ACCESS-ESM1-5 model and SCF scenario. Also, the lowest rate of ETo changes was predicted to be 1.79% and 0.84%, respectively, by the MRI-ESM2-0 and CanESM5 models and SCM scenarios. In Mianeh stations, the highest rate of ETo changes was predicted to be 2.20% by the CanESM5 model and SCF scenario. The lowest rate of ETo changes was predicted with the ACCESS-ESM1-5 model and SCM scenario of 0.68%. In the Mahabad station, the largest changes (1.66%) were predicted by the CanESM5 model and SCF scenario. However, the least ETo changes (0.50%) were related to the ACCESS-ESM1-5 model and SCM scenario. In Saqez and Takab stations, the highest rate of ETo changes were 2.80% and 2.70%, respectively, by the MRI-ESM2-0 model and SCF scenario and CanESM5 model and SCM scenario. The lowest ETo change rates of 0.87% and 1.04% were predicted by the ACCESS-ESM1-5 model and SCM scenario, respectively. In Zanjan stations, the highest rate of ETo changes was predicted with the CanESM5 model and SCF scenario of 3.44%. The lowest rate of ETo changes was predicted by the ACCESS-ESM1-5 model and SCM scenario of 0.64%.

**Table 8.** Results of prediction ETo at the different stations.

	A-SCF	A-SCM	A-SCS	C-SCF	C-SCM	C-SCS	M-SCF	M-SCM	M-SCS
Tabriz									
Mean-Obs	2.38	2.38	2.38	2.38	2.38	2.38	2.38	2.38	2.38
Mean-Pred	2.44	2.42	2.44	2.44	2.43	2.43	2.44	2.41	2.41
Min-Obs	0.39	0.39	0.39	0.39	0.39	0.39	0.39	0.39	0.39
Min-Pred	0.41	0.41	0.42	0.41	0.43	0.40	0.43	0.40	0.42
Max-Obs	4.85	4.85	4.85	4.85	4.85	4.85	4.85	4.85	4.85
Max-Pred	4.71	4.72	4.72	4.69	4.68	4.71	4.74	4.73	4.74
Change mean (%)	2.91	1.99	2.73	2.66	2.25	2.46	2.68	1.56	1.43
Urmia									
Mean-Obs	2.37	2.37	2.37	2.37	2.37	2.37	2.37	2.37	2.37
Mean-Pred	2.46	2.44	2.45	2.44	2.43	2.43	2.44	2.42	2.41
Min-Obs	0.44	0.44	0.44	0.44	0.44	0.44	0.44	0.44	0.44
Min-Pred	0.48	0.47	0.47	0.48	0.48	0.48	0.47	0.48	0.48
Max-Obs	4.98	4.98	4.98	4.98	4.98	4.98	4.98	4.98	4.98
Max-Pred	4.78	4.83	4.80	4.80	4.79	4.80	4.78	4.82	4.82
Change mean (%)	3.84	2.76	3.44	2.91	2.40	2.26	2.68	1.79	1.53
Mahabad									
Mean-Obs	2.40	2.40	2.40	2.40	2.40	2.40	2.40	2.40	2.40
Mean-Pred	2.44	2.41	2.42	2.44	2.41	2.42	2.43	2.43	2.42
Min-Obs	0.50	0.50	0.50	0.50	0.50	0.50	0.50	0.50	0.50
Min-Pred	0.56	0.55	0.55	0.53	0.53	0.53	0.52	0.54	0.52
Max-Obs	4.86	4.86	4.86	4.86	4.86	4.86	4.86	4.86	4.86
Max-Pred	4.79	4.75	4.79	4.75	4.70	4.75	4.73	4.73	4.75
Change mean (%)	1.57	0.50	0.87	1.66	0.69	1.07	1.53	1.30	1.03

Since the rate of ETo and its prediction in the future is a very important issue, according to the results of Table 8, optimistic and pessimistic situations can be identified at different stations. The smaller the mean change, the more optimistic the predicted amount of ETo in the future. The larger the average change, the more pessimistic the projected ETo rate is in the future. In order to better observe future ETo changes, the yearly change of mean daily ETo in historical and future periods is shown in Figures 6 and A9 (Appendix B.8). These figures are based on the results of the best algorithm (LSBoost) and SCF, SCM and SCS scenarios. ETo in all stations under all scenarios has increased.

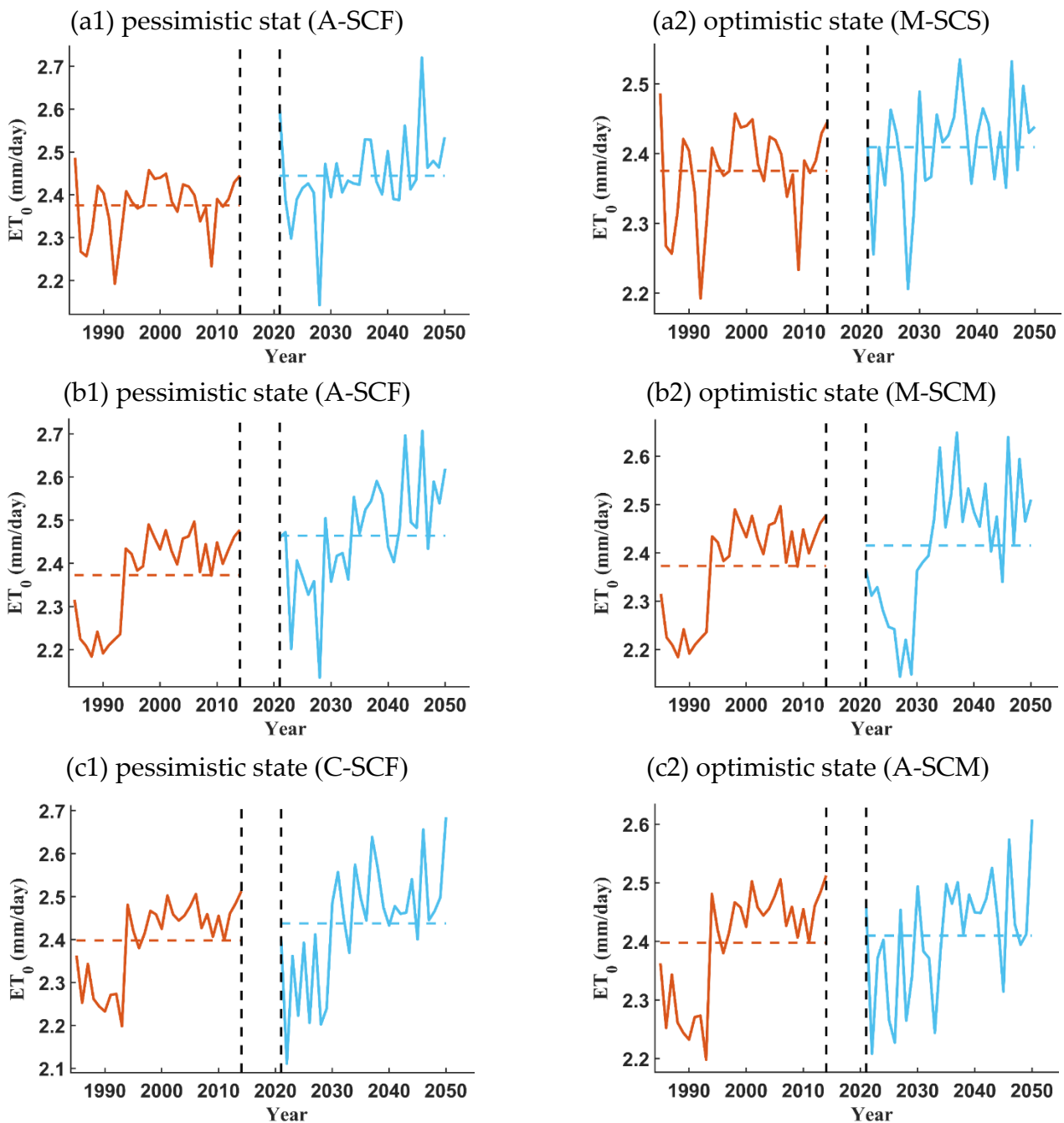


**Figure 6.** Pessimistic and optimistic predictions of ETo. (a1,a2) Tabriz, (b1,b2) Urmia, (c1,c2) Mahabad.

Furthermore, the changes in mean daily ETo in the initial years of the future period were descending while those for the last years of the future period were increasing. Also, in most stations, the amount of ETo increased in the SCF scenario and the ACCESS-ESM1-5

and CanESM5 models. These variations in GCMs and emission scenarios can be for different assumptions of those, negative feedbacks of climate change conditions and positive feedbacks of COVID-19. The highest increase is for the ACCESS-ESM1-5 model and SCF scenario in Urmia station's 2021–2050 period. The lowest is for the ACCESS-ESM1-5 model and SCM scenario in the 2021–2050 period in Mahabad station. These different results can be due to increased temperature and changes in wind speed and relative humidity, or other reasons.

### 3.5. Uncertainty Analysis

The uncertainty analysis based on the MCM for different stations and scenarios is given in Tables 9 and A5 (Appendix B.9). The results of this method are obtained based on random sampling. The MCM calculates a 95% confidence interval of the prediction uncertainty (95PPU). A lower R-factor coefficient indicates less uncertainty in the prediction scenarios. In the 2021–2050 horizon, the MRI-ESM2-0 model and SCM scenario in the Tabriz station had less uncertainty (for this model and scenario, the amount of ETo increased by 1.21%, which was more likely than other models and scenarios). In Urmia station, the MRI-ESM2-0 model and SCM scenario had a lower R-factor coefficient (in this model and scenario, the amount of ETo increased by 1.81%, which had more certainty than other models and scenarios). In Mahabad station, the MRI-ESM2-0 model and SCS scenario had a lower R-factor coefficient (in this model and scenario, the amount of ETo increased by 2.40%, which had more certainty than other models and scenarios). The uncertainty analysis results of other stations are stated in Appendix B.9. Figures 7 and A10 (Appendix B.10) show the uncertainty analysis results of the models and scenarios with the least uncertainty. The shaded region (95PPU) shows the upper and lower band results of the ETo values predicted for the 1000 new time series. More minor differences between the upper and lower bands indicate less uncertainty in the models and prediction scenarios. The results showed high uncertainty of GCMs and emission scenarios of CMIP6. However, based on the uncertainty analysis, the lowest uncertainty was related to the Mianeh station, and the highest uncertainty was related to the Mahabad station. Also, the MRI-ESM2-0 model and SCS scenario had the lowest uncertainty.

**Table 9.** Results of uncertainty evaluation by MCM at the different stations.

	R-Factor								
	A-SCF	A-SCM	A-SCS	C-SCF	C-SCM	C-SCS	M-SCF	M-SCM	M-SCS
Tabriz	2.481	2.476	2.474	2.465	2.461	2.464	2.462	2.460	2.463
Urmia	2.690	2.694	2.681	2.680	2.682	2.684	2.679	2.674	2.681
Mahabad	2.842	2.849	2.834	2.838	2.835	2.836	2.828	2.832	2.824

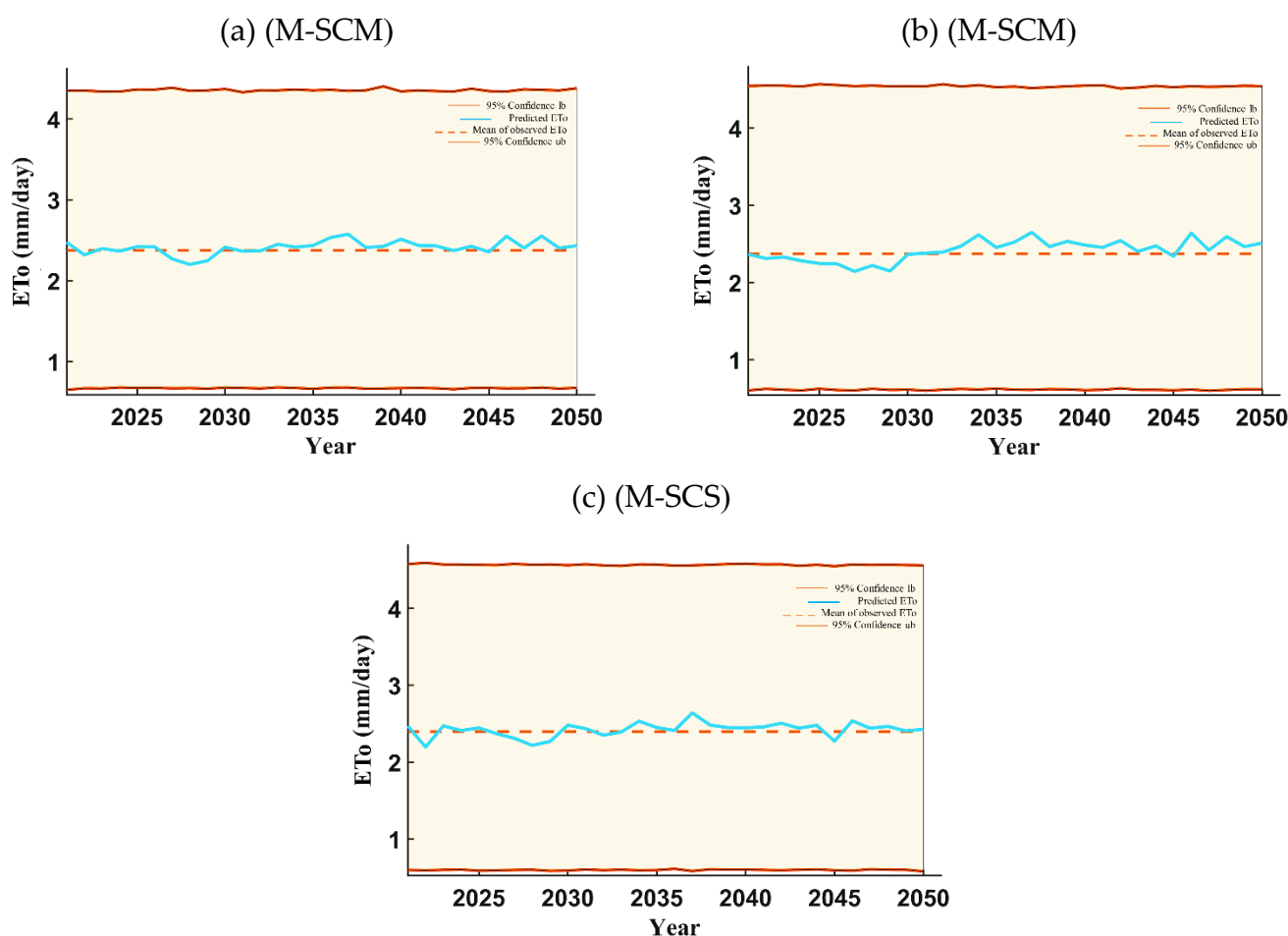


**Figure 7.** The uncertainty bound for GCMs and scenarios with less uncertainty. (a) Tabriz, (b) Urmia, (c) Mahabad.

#### 4. Conclusions

The present study predicted the future ETo in the two basins of Lake Urmia and Sefidrood using ACCESS-ESM1-5, CanESM5 and MRI-ESM2-0 models and SCF, SCM and SCS scenarios. The ETo was modeled using MLR, MNLR, MARS, M5, RF and LSBoost. The best algorithm was selected by the TOPSIS method. The monthly T and P data were downscaled using the delta CF method. Previous studies have used machine learning algorithms to predict ETo considering climate change conditions [16–18]. However, the present study used a new combination methodology for predicting ETo considering climate change and post-pandemic COVID-19. The results were investigated for historical (1985–2014) and future (2021–2050) periods. Through this study, the major conclusions are as follows:

1. The accuracy of machine learning algorithms for ETo modeling was very good. However, TOPSIS results showed that LSBoost (score = 0.96) was the best algorithm. The average evaluation criteria obtained by LSBoost in the nine stations were in a very good range (MAE = 0.18, RMSE = 0.06, R = 0.99, MARE = 0.11, RRMSE = 0.04, Time = 1.11 s).
2. Downscaling results showed that future monthly changes of mean T and P at all stations and scenarios increased. The highest increase in T was related to the Zanjan station in the CanESM5 model and SCF scenario (0.83 °C). In addition, the highest increase of P (11.20 mm/day) was related to the Mianeh station in the CanESM5 model and SCS scenario.

3. The mean amount of ETo in all stations increased in all models and scenarios. The highest increase was related to the Urmia station (3.84%), and the lowest was the Mahabad station (0.50%).
4. The GCMs and scenarios of CMIP6 had high uncertainty. However, for considered GCMs and scenarios, the lowest and highest uncertainty in the MRI-ESM2-0 model and SCS scenario were in the Mianeh (R-factor = 1.979) and Mahabad (R-factor = 2.824) stations, respectively.

ETo is a critical component of the hydrological cycle that has important effects on the quantity and quality of water resources in agriculture and industry. For sustainable water resources management, prediction of ETo under probable scenarios is an essential step. This methodology can be extended to other new GCMs and emission scenarios from CMIP6. Evapotranspiration of other plants can be estimated using ETo.

**Author Contributions:** Conceptualization, S.F.; Data curation, M.K., M.V.A. and A.M.-B.; Formal analysis, M.K., M.V.A., A.M.-B. and S.F.; Investigation, M.K., M.V.A. and S.F.; Methodology, M.K., M.V.A., A.M.-B. and S.F.; Project administration, S.F.; Resources, M.K., M.V.A. and A.M.-B.; Software, M.K., M.V.A. and A.M.-B.; Supervision, S.F.; Validation, M.K., M.V.A. and A.M.-B.; Visualization, M.K., M.V.A. and A.M.-B.; Writing—original draft, M.K., M.V.A. and A.M.-B.; Writing—review and editing, S.F. All authors have read and agreed to the published version of the manuscript.

**Funding:** The research has not been supported through any funds.

**Institutional Review Board Statement:** Not applicable.

**Informed Consent Statement:** Not applicable.

**Data Availability Statement:** All data generated or used during the study are applicable if requested.

**Conflicts of Interest:** The authors declare that they have no conflict of interest.

## Appendix A

### Appendix A.1

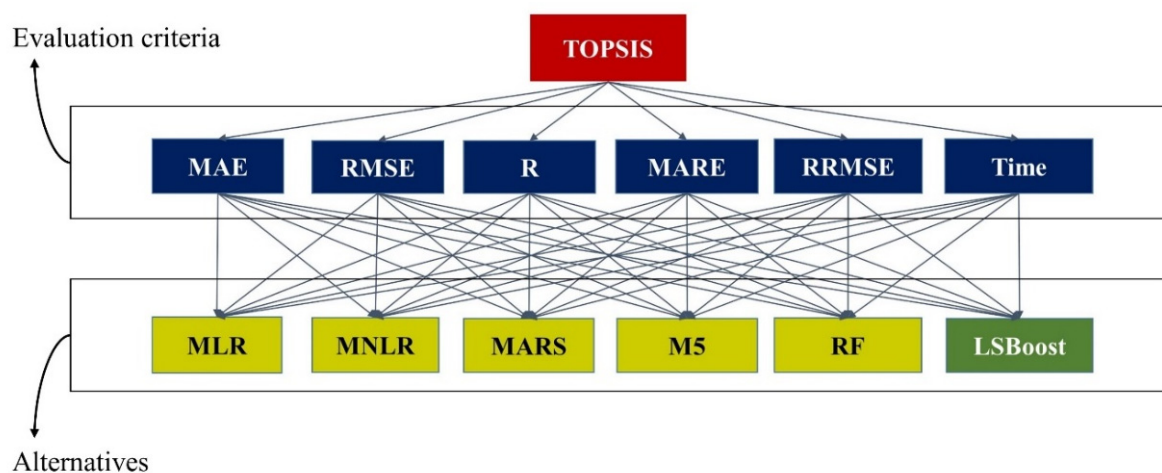


**Figure A1.** TOPSIS structure for selecting best algorithm.

### Appendix A.2

$$E_{To} = \frac{0.408 \Delta (R_n - G) + \gamma \frac{900}{T+273} u_2 (e_s - e_a)}{\Delta + \gamma(1 + 0.34u_2)} \quad (A1)$$

where  $R_n$  is the net radiation ( $\text{MJ}/\text{m}^2/\text{day}$ ),  $\Delta$  is the slope of saturation vapor pressure curve ( $\text{kPa}/^\circ\text{C}$ ),  $G$  is soil heat flux ( $\text{MJ}/\text{m}^2/\text{day}$ ),  $e_s$  and  $e_a$  are saturated and actual vapor

pressures (kPa),  $\gamma$  is psychrometric constant (kPa/°C),  $U$  is the monthly wind speed at 2 m height (m/s) and  $T$  is the mean air temperature (°C).

Appendix A.3

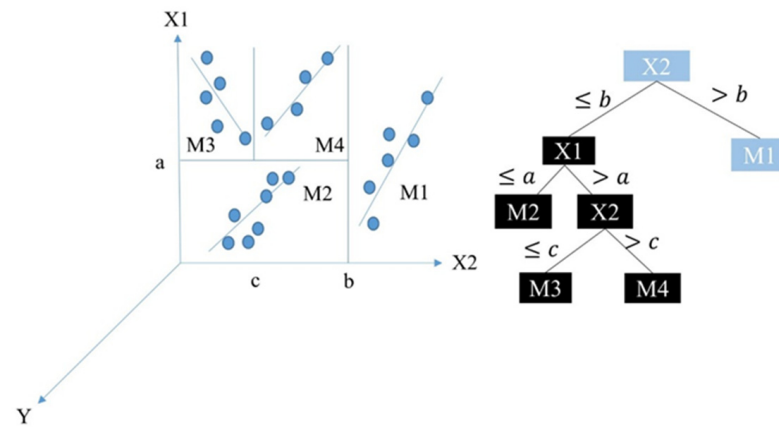


Figure A2. The schematic structure of M5 model.

Appendix A.4

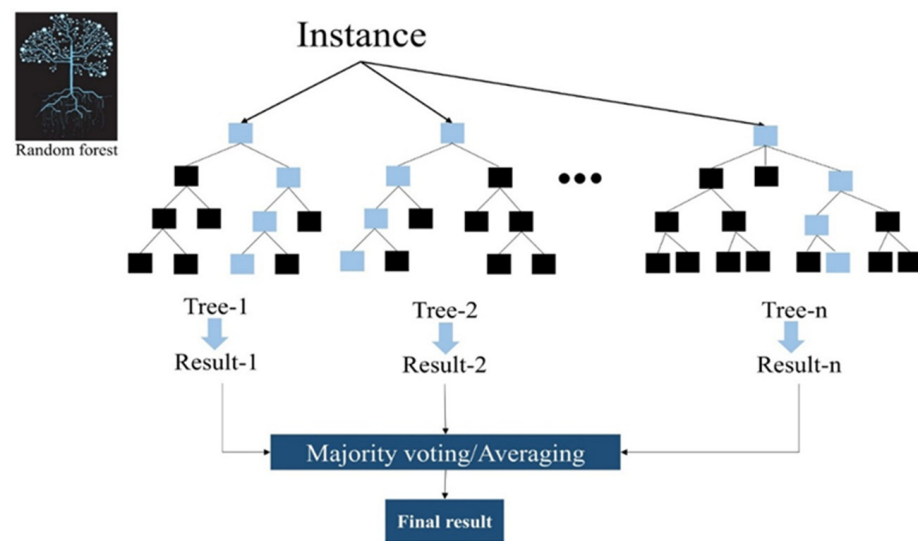


Figure A3. The schematic structure of RF model.

Appendix A.5

In the TOPSIS method first, the decision matrixes are created based on the n alternative and m criteria as follows:

$$A = \begin{bmatrix} d_{11} & d_{12} & \dots & d_{1n} \\ d_{21} & d_{22} & \dots & d_{2n} \\ \vdots & \vdots & \vdots & \vdots \\ d_{m1} & d_{m2} & \dots & d_{mn} \end{bmatrix} \tag{A2}$$

where  $d_{ij}$  is the element of decision matrix. Next, the decision matrix ( $r$ ) is normalized as follows:

$$r = \begin{bmatrix} \frac{d_{11}}{\sqrt{\sum_{i=1}^m d_{ij}}} & \frac{d_{12}}{\sqrt{\sum_{i=1}^m d_{ij}}} & \dots & \frac{d_{1n}}{\sqrt{\sum_{i=1}^m d_{ij}}} \\ \frac{d_{21}}{\sqrt{\sum_{i=1}^m d_{ij}}} & \frac{d_{22}}{\sqrt{\sum_{i=1}^m d_{ij}}} & \dots & \frac{d_{2n}}{\sqrt{\sum_{i=1}^m d_{ij}}} \\ \vdots & \vdots & \ddots & \vdots \\ \frac{d_{m1}}{\sqrt{\sum_{i=1}^m d_{ij}}} & \frac{d_{m2}}{\sqrt{\sum_{i=1}^m d_{ij}}} & \dots & \frac{d_{mn}}{\sqrt{\sum_{i=1}^m d_{ij}}} \end{bmatrix} \tag{A3}$$

Then, the weighted normalized decision matrix ( $V$ ) is generated as follows:

$$V_{mn} = (W_j * r_{ij})_{mn} \tag{A4}$$

In the next step, the PIS and NIS are calculated by the following equations:

$$PIS = [a_1^+, a_2^+, a_3^+, \dots, a_n^+] = \max\{v_{ij} \mid i = 1, 2, 3, \dots, m\} \tag{A5}$$

$$NIS = [a_1^-, a_2^-, a_3^-, \dots, a_n^-] = \min\{v_{ij} \mid i = 1, 2, 3, \dots, m\} \tag{A6}$$

Finally, the score of each alternative is calculated as follows:

$$Score_i^+ = \frac{\sqrt{(v_{ij} - a_j^-)}}{\sqrt{(v_{ij} - a_j^-)} + \sqrt{(v_{ij} - a_j^+)}} \tag{A7}$$

Appendix A.6

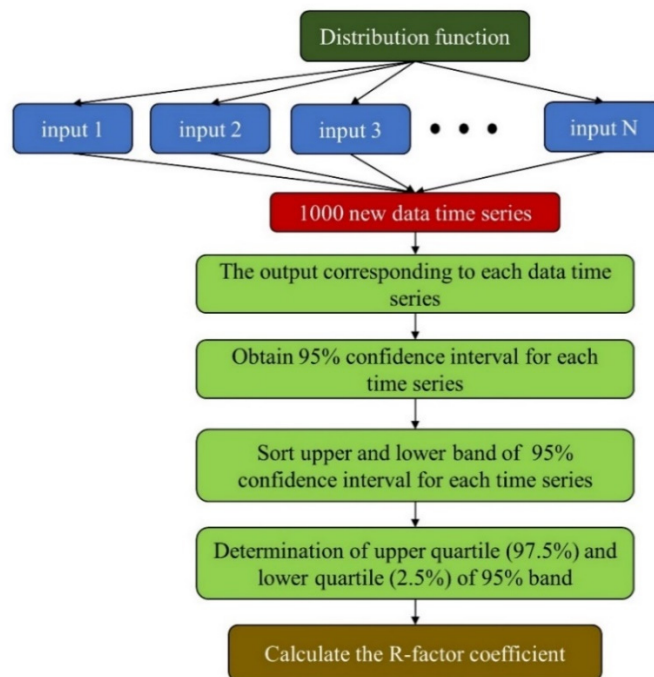


Figure A4. Steps of the MCM.

## Appendix A.7

$$\text{MAE} = \frac{\sum_{i=1}^N |Y_i - \hat{Y}_i|}{N} \quad (\text{A8})$$

$$\text{RMSE} = \sqrt{\frac{\sum_{i=1}^N (Y_i - \hat{Y}_i)^2}{N}} \quad (\text{A9})$$

$$R = \frac{\sum_{i=1}^N (Y_i - \bar{Y}_i)(\hat{Y}_i - \hat{\bar{Y}}_i)}{\sqrt{\sum_{i=1}^N (Y_i - \bar{Y}_i)^2 \sum_{i=1}^N (\hat{Y}_i - \hat{\bar{Y}}_i)^2}} \quad (\text{A10})$$

$$\text{MARE} = \frac{\sum_{i=1}^N \frac{|Y_i - \hat{Y}_i|}{Y_i}}{N} \quad (\text{A11})$$

$$\text{RRMSE} = \frac{\text{RMSE}}{\hat{\text{Std}}} \quad (\text{A12})$$

where  $Y_i$ ,  $\hat{Y}_i$ ,  $\hat{\text{Std}}$  and  $N$  are the modeled ETo, observed ETo, standard deviation of ETo and number of ETo samples. The MAE, RMSE, MARE and RRMSE are in the range of zero to infinite positive numbers, and the desirable values are zero. Furthermore, the  $R$  is in the range of zero to one, and the best value is one.

## Appendix A.8

Table A1. The mean and standard deviation of inputs and targets.

Station	Basin	Parameter	Min T (°C)	Mean T (°C)	Max T (°C)	Humidity (%)	Wind Speed (m/s)	P (mm/Month)	ETo (mm/Day)
Tabriz	Urmia	Std	7.78	12.84	18.84	51.23	3.12	20.89	7.81
		Mean	8.72	9.94	10.76	14.25	1.01	19.58	2.37
Sahand	Urmia	Std	7.40	12.00	16.96	49.74	3.73	19.16	8.06
		Mean	8.08	9.37	10.19	13.23	1.92	18.50	2.36
Urmia	Urmia	Std	5.36	11.33	17.94	58.93	1.86	26.28	8.13
		Mean	7.44	9.13	9.86	11.24	0.86	28.07	2.37
Maragheh	Urmia	Std	8.14	12.87	18.90	49.32	2.72	25.13	8.10
		Mean	8.15	9.66	10.49	14.86	1.29	26.84	2.38
Mianeh	Sefidrood	Std	7.69	14.04	20.62	51.71	1.80	23.49	7.97
		Mean	7.96	10.59	10.97	14.61	0.97	22.13	2.42
Mahabad	Urmia	Std	7.18	13.06	19.41	52.29	2.08	33.59	8.03
		Mean	7.10	9.33	10.35	14.94	0.87	34.65	2.40
Saqez	Urmia	Std	3.03	11.36	18.94	53.75	2.16	38.37	8.20
		Mean	7.08	9.71	10.96	17.36	0.95	40.96	2.38
Takab	Urmia	Std	2.53	10.12	16.48	54.24	2.13	25.87	8.00
		Mean	7.38	9.80	10.80	16.72	0.90	24.26	2.33
Zanjan	Sefidrood	Std	2.13	8.71	14.89	53.93	3.59	32.02	8.38
		Mean	7.33	9.19	10.09	16.73	1.15	31.15	2.32

## *Appendix A.9*

### *Appendix A.9.1 Fossil-Fueled Recovery*

Following the two-year blip path from June 2020 until the end of 2021, emissions recover in a manner comparable to the recovery from the 2008 global recession, returning to 4.5 percent over the baseline by the end of 2022. The stimulus packages are aimed to boost fossil-fuel energy supplies, resulting in a 1% increase in fossil investment and a 0.8 percent decrease in low-carbon alternatives. The resulting emissions are 10% higher in 2030 than the baseline scenario, and this trend is expected to continue.

### *Appendix A.9.2 Moderate Green Stimulus*

Following the two-year blip path from June 2020 until the end of 2021, emissions recover marginally until 2022 but never approach the baseline forecasts. Governments choose recovery packages that focus on low-carbon energy supply and efficiency, not fossil-fuel bailouts. A 35 percent reduction in GHG emissions relative to the baseline scenario by 2030 is assumed to continue after that, consistent with reaching global net-zero CO<sub>2</sub> by 2060.

### *Appendix A.9.3 Strong Green Stimulus*

In terms of the moderate green stimulus, investment differentials (+1.2% for low-carbon technologies and 0.4% for fossil fuels relative to a current-policy scenario) result in a slightly more than 50% reduction in GHG emissions by 2030 relative to the baseline scenario. This trend is expected to continue in order to achieve global net-zero CO<sub>2</sub> emissions by 2050.

## **Appendix B**

### *Appendix B.1*

In the Sahand station, the RF model provided good results too. The lowest value of MAE, RMSE, MARE and RRMSE were equal to 0.19, 0.06, 0.13 and 0.04, respectively, and the highest value of R was equal to 0.99. The Maragheh station showed that the LSBoost model provided much better accuracy than the other models. Values of MAE, RMSE, R, MARE and RRMSE were 0.19, 0.06, 0.99, 0.13 and 0.04, respectively. In terms of MAE, RMSE, R, MARE and RRMSE in Mianeh station, the LSBoost model (0.14, 0.03, 0.99, 0.09, 0.02, respectively), and in Saqez station, the LSBoost model (0.15, 0.04, 0.99, 0.11, 0.03, respectively) produced better estimation accuracy in modeling ETo than the other machine learning models. Also, in Takab station the MARS model showed the highest modeling accuracy. The value of MAE was equal to 0.19, RMSE equal to 0.05, R equal to 0.99, MARE equal to 0.11 and RRMSE equal to 0.04. In the Zanjan station, results showed that the RF model provided much better accuracy than the other models. The value of MAE was equal to 0.16, RMSE equal to 0.05, R equal to 0.99, MARE equal to 0.11 and RRMSE equal to 0.03.

**Table A2.** Results of the algorithms to the ETo modeling at the different stations.

	Train					Test				
					Sahand					
	MAE	RMSE	R	MARE	RRMSE	MAE	RMSE	R	MARE	RRMSE
MLR	0.40	0.27	0.93	0.32	0.18	0.28	0.13	0.97	0.24	0.08
MNLR	0.33	0.21	0.95	0.23	0.14	0.25	0.09	0.98	0.17	0.06
MARS	0.33	0.22	0.95	0.22	0.15	0.24	0.08	0.98	0.15	0.06
M5	0.22	0.16	0.96	0.16	0.11	0.23	0.16	0.97	0.17	0.10
RF	0.21	0.14	0.97	0.15	0.10	0.19	0.06	0.99	0.13	0.04
LSBoost	0.15	0.13	0.97	0.12	0.09	0.20	0.07	0.98	0.14	0.05
					Maragheh					
MLR	0.25	0.10	0.97	0.17	0.07	0.56	1.11	0.78	0.35	0.73
MNLR	0.19	0.07	0.98	0.12	0.05	0.50	1.06	0.79	0.27	0.69
MARS	0.23	0.08	0.98	0.14	0.06	0.23	0.07	0.99	0.16	0.05
M5	0.10	0.02	0.99	0.05	0.02	0.20	0.07	0.98	0.12	0.05
RF	0.13	0.03	0.99	0.07	0.02	0.22	0.08	0.99	0.15	0.05
LSBoost	0.02	0.00	1.00	0.01	0.00	0.19	0.06	0.99	0.13	0.04
					Mianeh					
MLR	0.32	0.20	0.95	0.27	0.13	0.56	1.14	0.79	0.36	0.74
MNLR	0.24	0.13	0.97	0.17	0.09	0.46	1.07	0.81	0.23	0.69
MARS	0.23	0.13	0.97	0.15	0.08	0.17	0.05	0.99	0.10	0.03
M5	0.12	0.09	0.98	0.08	0.06	0.15	0.05	0.99	0.10	0.03
RF	0.16	0.11	0.98	0.12	0.07	0.15	0.04	0.99	0.09	0.02
LSBoost	0.13	0.09	0.98	0.10	0.06	0.14	0.03	0.99	0.09	0.02
					Saqez					
MLR	0.30	0.14	0.99	0.23	0.10	0.31	0.15	0.97	0.26	0.10
MNLR	0.23	0.08	0.98	0.15	0.06	0.24	0.08	0.98	0.18	0.06
MARS	0.18	0.05	0.99	0.11	0.04	0.20	0.06	0.98	0.14	0.04
M5	0.12	0.03	0.99	0.07	0.02	0.16	0.09	0.98	0.09	0.06
RF	0.11	0.02	0.99	0.07	0.02	0.17	0.05	0.99	0.12	0.03
LSBoost	0.02	0.00	1.00	0.02	0.00	0.15	0.04	0.99	0.11	0.03
					Takab					
MLR	0.28	0.14	0.96	0.21	0.10	0.26	0.09	0.98	0.20	0.07
MNLR	0.24	0.11	0.97	0.16	0.08	0.22	0.06	0.98	0.15	0.05
MARS	0.19	0.08	0.98	0.12	0.06	0.19	0.05	0.99	0.11	0.04
M5	0.13	0.06	0.98	0.08	0.04	0.22	0.13	0.97	0.13	0.09
RF	0.13	0.06	0.99	0.08	0.04	0.20	0.07	0.98	0.12	0.05
LSBoost	0.07	0.04	0.99	0.05	0.03	0.21	0.09	0.98	0.13	0.06
					Zanjan					
MLR	0.39	0.27	0.92	0.28	0.20	0.29	0.12	0.97	0.22	0.08
MNLR	0.34	0.24	0.93	0.22	0.18	0.22	0.07	0.98	0.14	0.05
MARS	0.31	0.22	0.94	0.21	0.16	0.22	0.07	0.99	0.14	0.05
M5	0.27	0.21	0.94	0.17	0.15	0.20	0.10	0.98	0.12	0.07
RF	0.25	0.19	0.94	0.16	0.15	0.16	0.05	0.99	0.11	0.03
LSBoost	0.31	0.22	0.94	0.18	0.16	0.20	0.07	0.98	0.12	0.05

## Appendix B.2

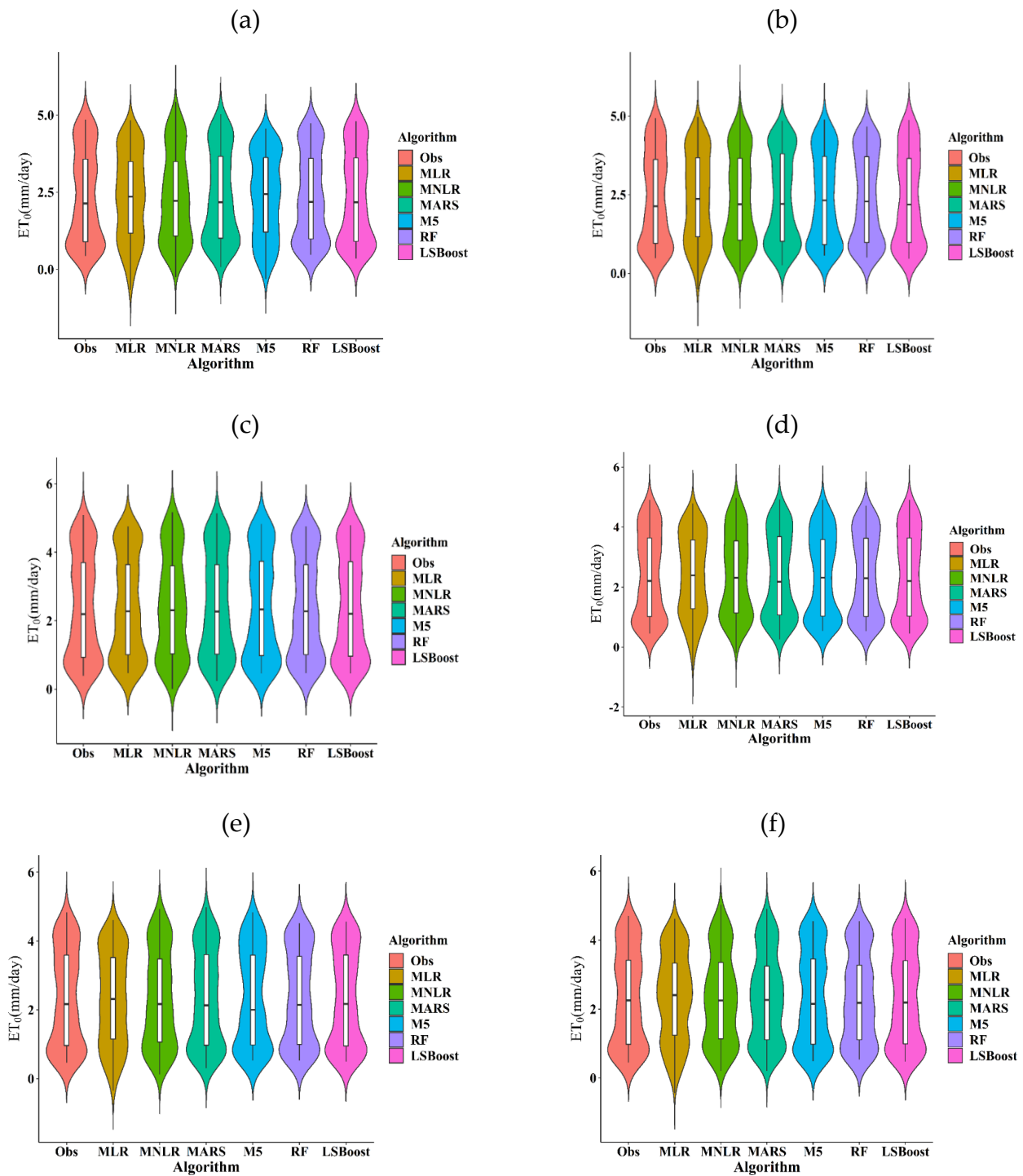


**Figure A5.** Violin plot of daily mean  $ET_0$  estimated by different models. (a) Sahand, (b) Maragheh, (c) Mianeh, (d) Saqez, (e) Takab, (f) Zanjan.

Appendix B.3

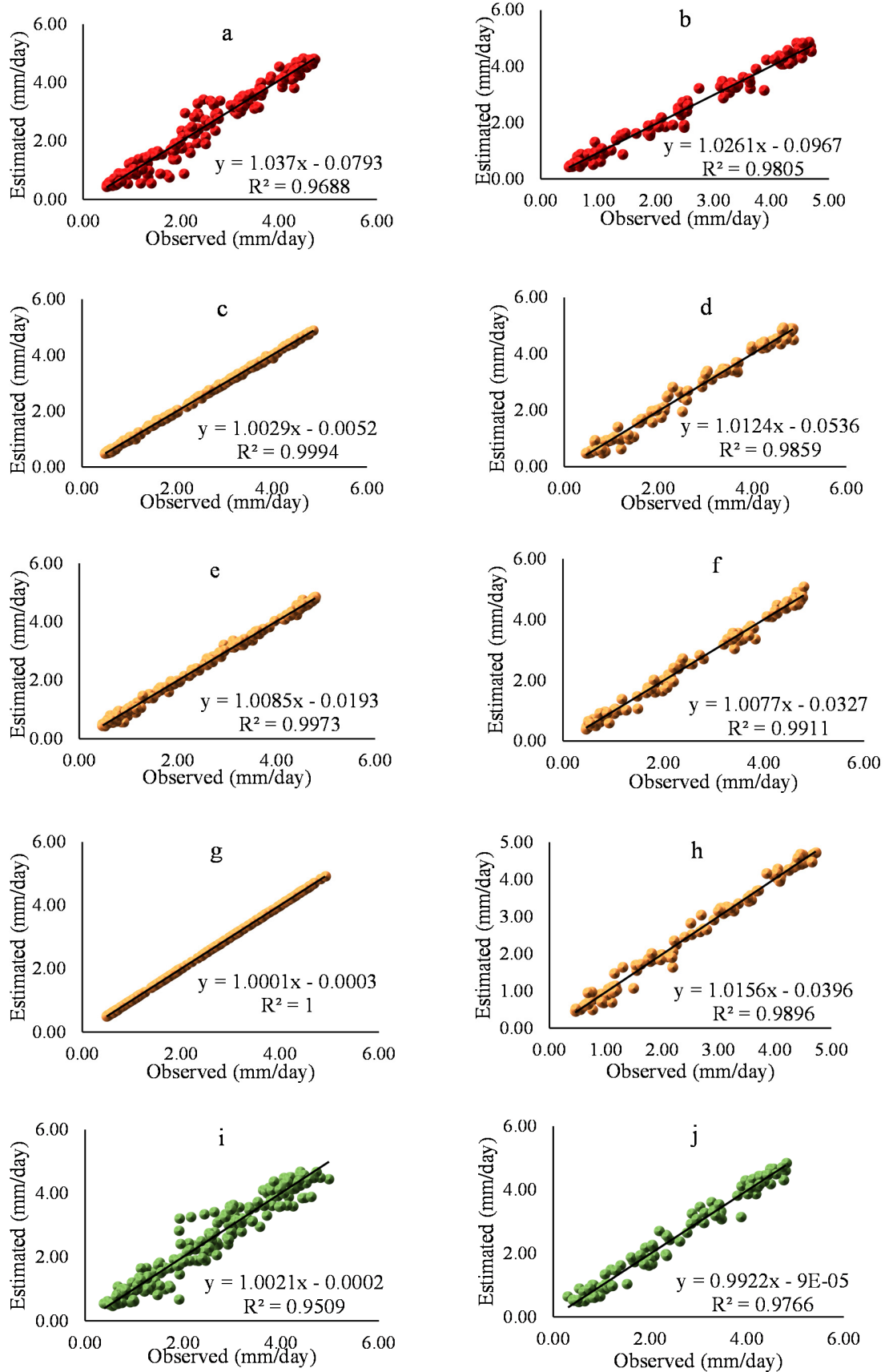
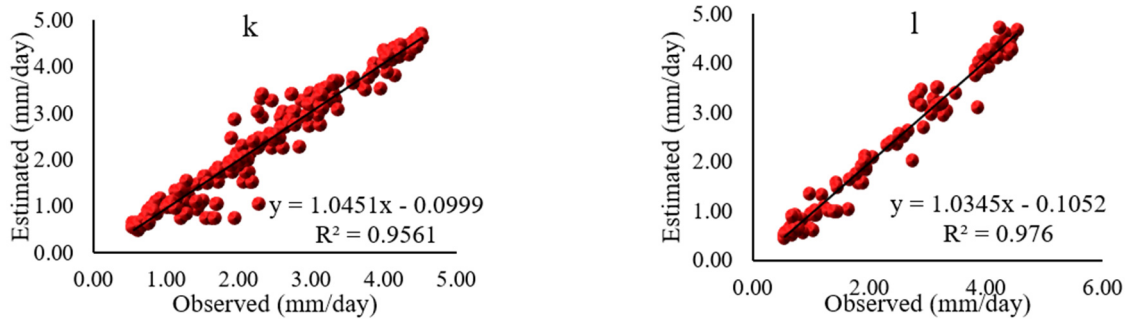
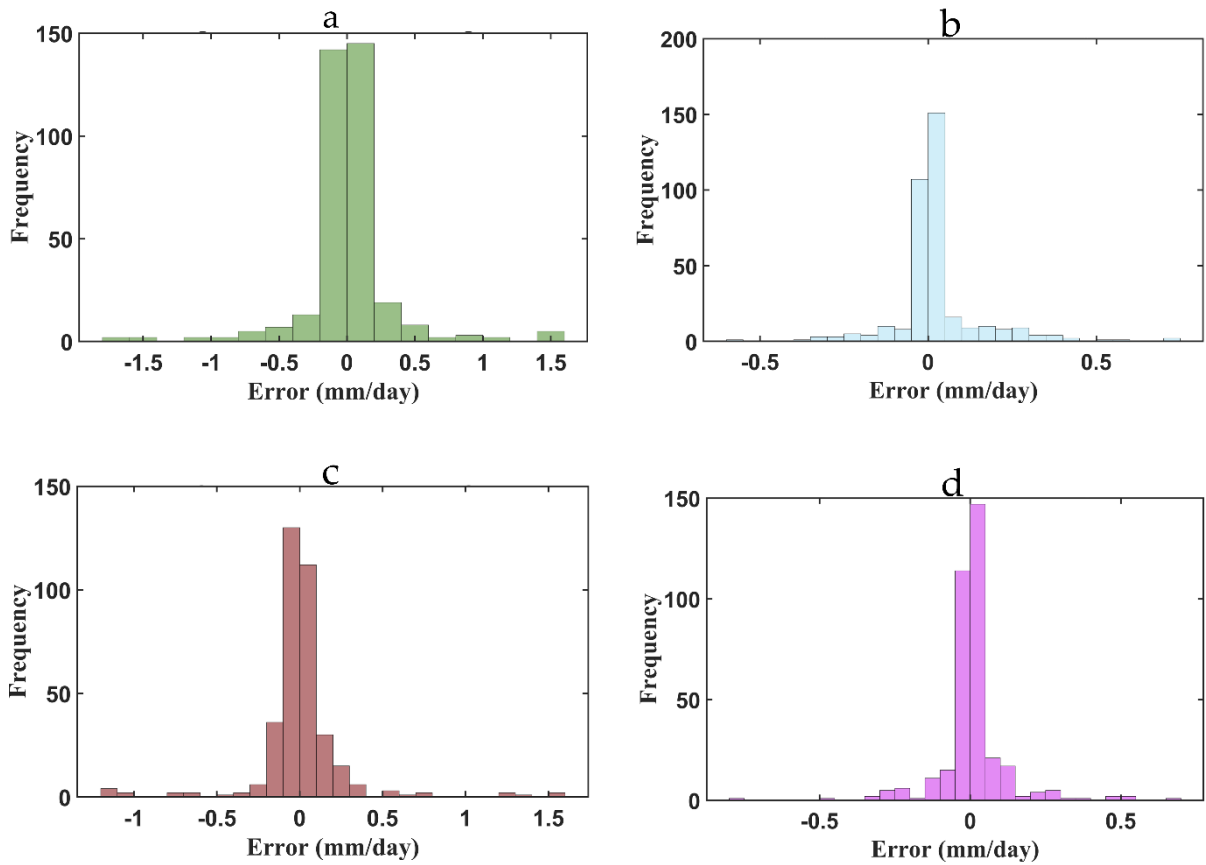


Figure A6. Cont.



**Figure A6.** The results of the scatter plots by the best algorithm. (a) Sahand-train, (b) Sahand-test, (c) Maragheh-train, (d) Maragheh-test, (e) Mianeh-train, (f) Mianeh-test, (g) Saqez-train, (h) Saqez-test, (i) Takab-train, (j) Takab-test, (k) Zanjan-train, (l) Zanjan-test.

*Appendix B.4*



**Figure A7.** *Cont.*

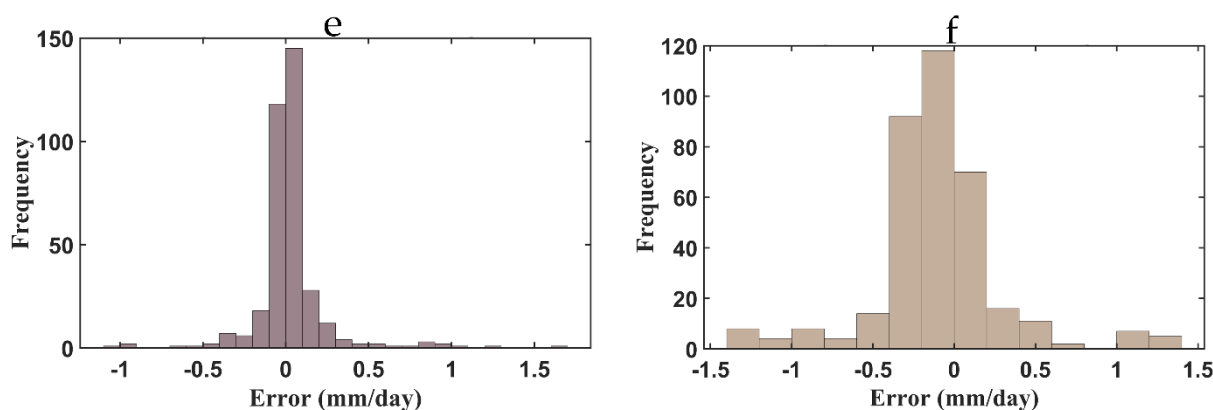


Figure A7. The histogram of the error in modeling ETo by the best algorithm. (a) Sahand, (b) Maragheh, (c) Mianeh, (d) Saqez, (e) Takab, (f) Zanzan.

Appendix B.5

Table A3. Downscaling of T and P at the different stations.

Station	Model-Scenario	$\Delta T$ ( $^{\circ}C$ )	$\Delta P$ (mm/Day)	Station	Model-Scenario	$\Delta T$ ( $^{\circ}C$ )	$\Delta P$ (mm/Day)
Sahand	A-SCF	0.53	2.35	Saqez	A-SCF	0.51	3.56
	A-SCM	0.34	1.84		A-SCM	0.32	3.23
	A-SCS	0.45	1.46		A-SCS	0.43	3.30
	C-SCF	0.69	2.37		C-SCF	0.71	3.95
	C-SCM	0.55	2.26		C-SCM	0.54	4.57
	C-SCS	0.53	2.29		C-SCS	0.52	2.46
	M-SCF	0.61	-0.09		M-SCF	0.60	-0.98
	M-SCM	0.45	1.43		M-SCM	0.44	3.10
Maragheh	M-SCS	0.42	-0.01	Takab	M-SCS	0.41	-1.43
	A-SCF	0.53	2.05		A-SCF	0.51	2.95
	A-SCM	0.34	1.61		A-SCM	0.32	2.78
	A-SCS	0.45	1.43		A-SCS	0.43	2.74
	C-SCF	0.69	2.31		C-SCF	0.78	6.70
	C-SCM	0.55	2.70		C-SCM	0.71	7.98
	C-SCS	0.53	2.66		C-SCS	0.63	10.94
	M-SCF	0.61	-0.30		M-SCF	0.63	-0.59
Mianeh	M-SCM	0.45	1.63	Zanzan	M-SCM	0.47	1.29
	M-SCS	0.42	-0.65		M-SCS	0.45	-0.35
	A-SCF	0.53	2.58		A-SCF	0.51	3.21
	A-SCM	0.34	2.47		A-SCM	0.32	3.20
	A-SCS	0.45	2.19		A-SCS	0.43	3.33
	C-SCF	0.78	6.65		C-SCF	0.83	6.01
	C-SCM	0.71	7.03		C-SCM	0.71	7.27
	C-SCS	0.63	11.20		C-SCS	0.62	7.58
M-SCF	0.64	0.66	M-SCF	0.63	-0.76		
M-SCM	0.49	2.23	M-SCM	0.47	1.42		
M-SCS	0.46	-0.09	M-SCS	0.45	-0.77		

Appendix B.6

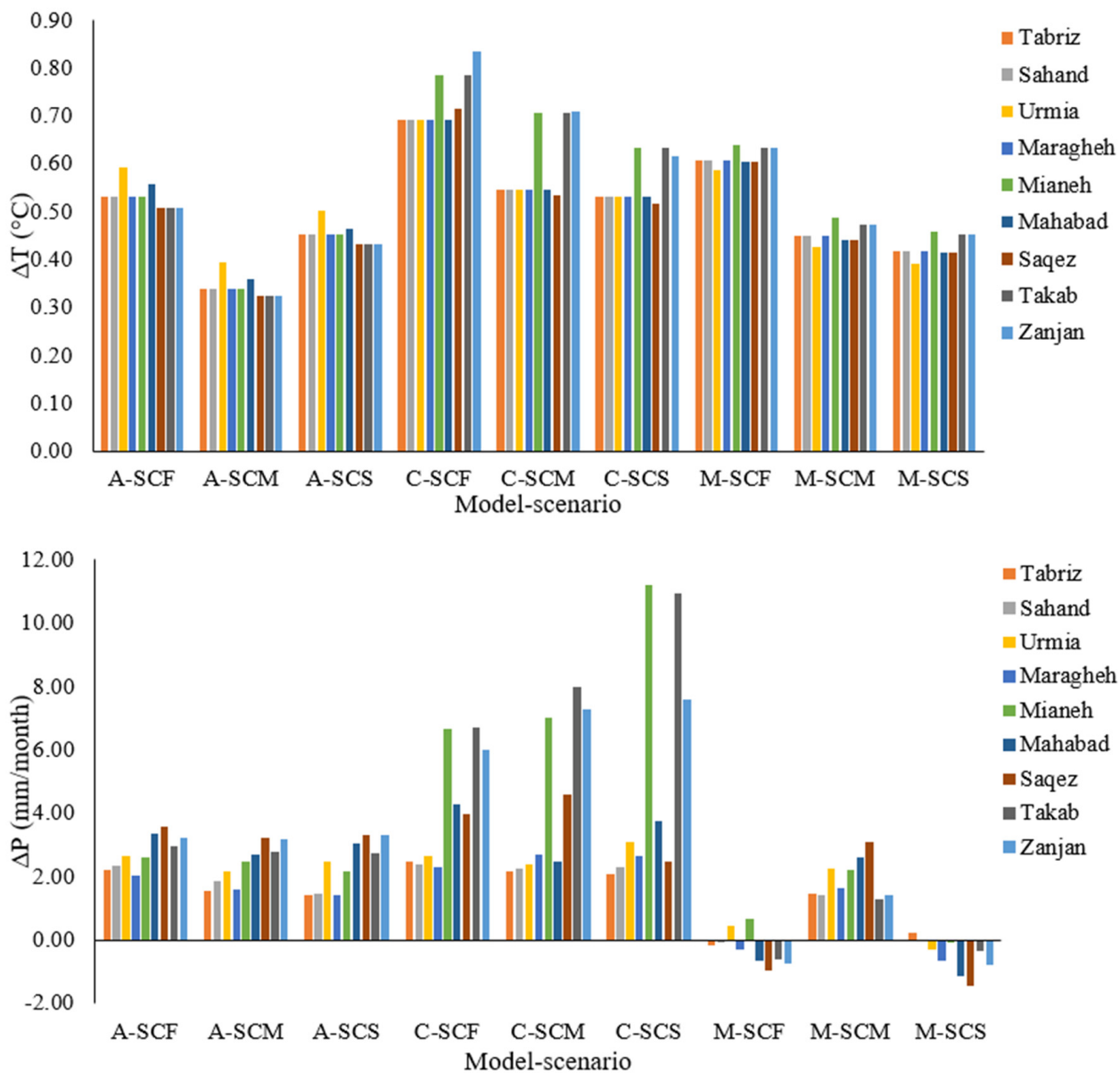


Figure A8. Downscaling of T and P at the different stations.

## Appendix B.7

Table A4. Results of prediction ETo at the different stations.

	A-SCF	A-SCM	A-SCS	C-SCF	C-SCM	C-SCS	M-SCF	M-SCM	M-SCS
Sahand									
Mean-Obs	2.36	2.36	2.36	2.36	2.36	2.36	2.36	2.36	2.36
Mean-Pred	2.44	2.41	2.43	2.44	2.42	2.42	2.41	2.41	2.41
Min-Obs	0.43	0.43	0.43	0.43	0.43	0.43	0.43	0.43	0.43
Min-Pred	0.39	0.37	0.35	0.36	0.32	0.38	0.36	0.36	0.36
Max-Obs	4.86	4.86	4.86	4.86	4.86	4.86	4.86	4.86	4.86
Max-Pred	4.83	4.80	4.78	4.86	4.83	4.82	4.80	4.81	4.79
Change mean (%)	3.28	1.83	2.69	3.03	2.55	2.31	2.08	1.84	2.09
Maragheh									
Mean-Obs	2.38	2.38	2.38	2.38	2.38	2.38	2.38	2.38	2.38
Mean-Pred	2.43	2.41	2.43	2.41	2.40	2.41	2.42	2.40	2.40
Min-Obs	0.48	0.48	0.48	0.48	0.48	0.48	0.48	0.48	0.48
Min-Pred	0.47	0.45	0.47	0.48	0.45	0.42	0.47	0.46	0.46
Max-Obs	4.93	4.93	4.93	4.93	4.93	4.93	4.93	4.93	4.93
Max-Pred	4.92	4.89	4.90	4.87	4.97	4.95	4.90	4.86	4.93
Change mean (%)	2.28	1.30	1.96	1.33	0.84	1.20	1.57	0.98	0.87
Mianeh									
Mean-Obs	2.42	2.42	2.42	2.42	2.42	2.42	2.42	2.42	2.42
Mean-Pred	2.47	2.44	2.46	2.48	2.46	2.46	2.47	2.45	2.45
Min-Obs	0.39	0.39	0.39	0.39	0.39	0.39	0.39	0.39	0.39
Min-Pred	0.38	0.39	0.41	0.45	0.40	0.39	0.39	0.46	0.37
Max-Obs	5.09	5.09	5.09	5.09	5.09	5.09	5.09	5.09	5.09
Max-Pred	4.84	4.87	4.89	4.88	4.82	4.81	4.83	4.84	4.84
Change mean (%)	1.93	0.68	1.36	2.20	1.77	1.70	1.85	1.11	1.29
Saqez									
Mean-Obs	2.38	2.38	2.38	2.38	2.38	2.38	2.38	2.38	2.38
Mean-Pred	2.43	2.40	2.44	2.44	2.43	2.43	2.45	2.43	2.42
Min-Obs	0.45	0.45	0.45	0.45	0.45	0.45	0.45	0.45	0.45
Min-Pred	0.46	0.46	0.46	0.46	0.36	0.42	0.44	0.43	0.46
Max-Obs	4.91	4.91	4.91	4.91	4.91	4.91	4.91	4.91	4.91
Max-Pred	4.87	4.86	4.86	4.87	4.92	4.84	4.93	4.88	4.93
Change mean (%)	2.06	0.87	2.38	2.65	1.91	2.16	2.80	1.98	1.69
Takab									
Mean-Obs	2.33	2.33	2.33	2.33	2.33	2.33	2.33	2.33	2.33
Mean-Pred	2.38	2.35	2.38	2.39	2.39	2.38	2.38	2.37	2.37
Min-Obs	0.47	0.47	0.47	0.47	0.47	0.47	0.47	0.47	0.47
Min-Pred	0.49	0.45	0.50	0.50	0.51	0.50	0.49	0.51	0.49
Max-Obs	4.84	4.84	4.84	4.84	4.84	4.84	4.84	4.84	4.84
Max-Pred	4.56	4.53	4.55	4.55	4.55	4.54	4.55	4.57	4.57
Change mean (%)	2.40	1.04	2.09	2.68	2.70	2.42	2.25	1.97	1.85
Zanjan									
Mean-Obs	2.32	2.32	2.32	2.32	2.32	2.32	2.32	2.32	2.32
Mean-Pred	2.35	2.34	2.34	2.40	2.38	2.37	2.39	2.36	2.36
Min-Obs	0.45	0.45	0.45	0.45	0.45	0.45	0.45	0.45	0.45
Min-Pred	0.51	0.48	0.52	0.52	0.52	0.50	0.48	0.48	0.48
Max-Obs	4.70	4.70	4.70	4.70	4.70	4.70	4.70	4.70	4.70
Max-Pred	4.57	4.57	4.57	4.54	4.54	4.54	4.58	4.56	4.57
Change mean (%)	1.27	0.64	0.85	3.44	2.41	2.01	2.88	1.58	1.70

Appendix B.8

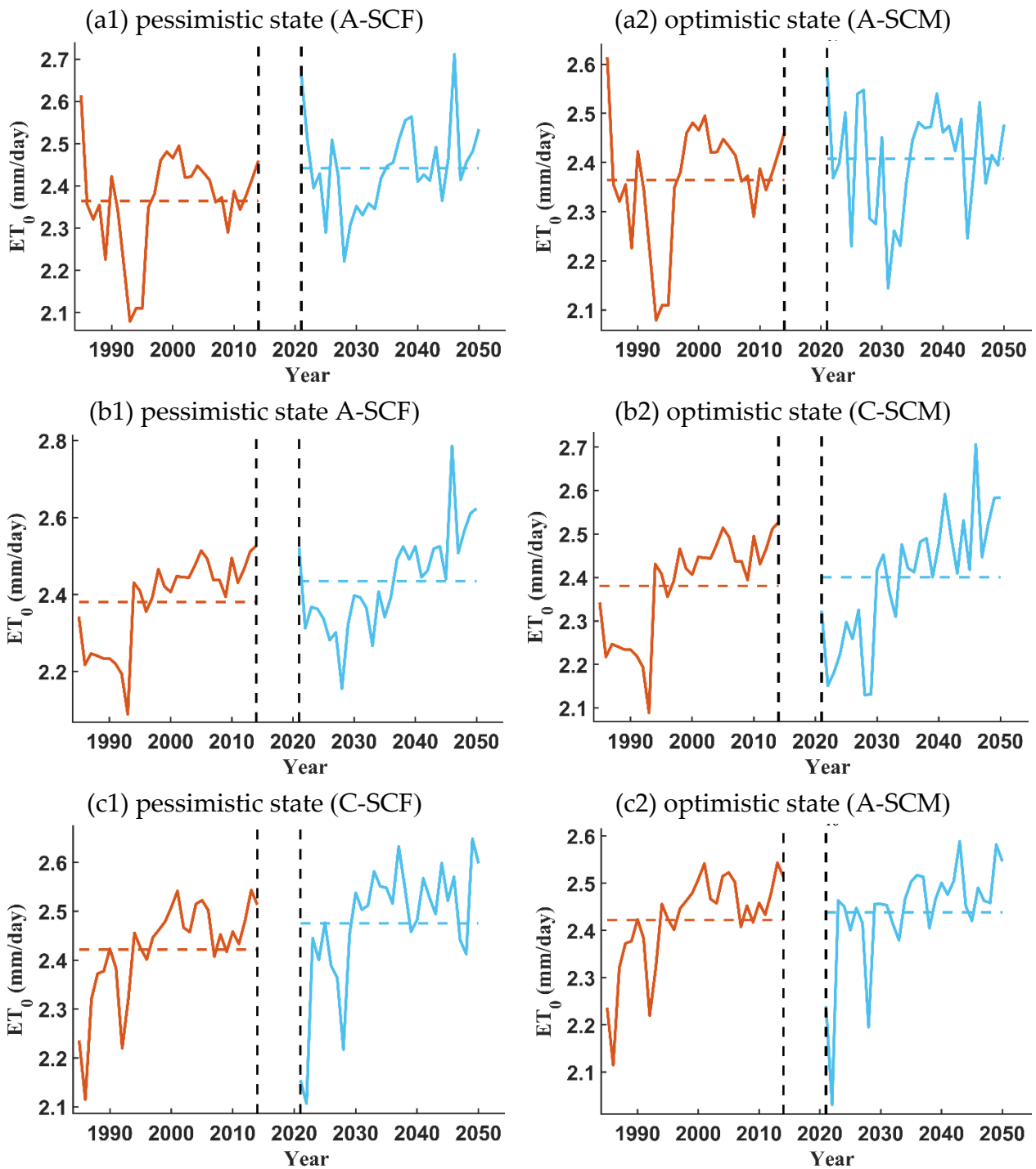
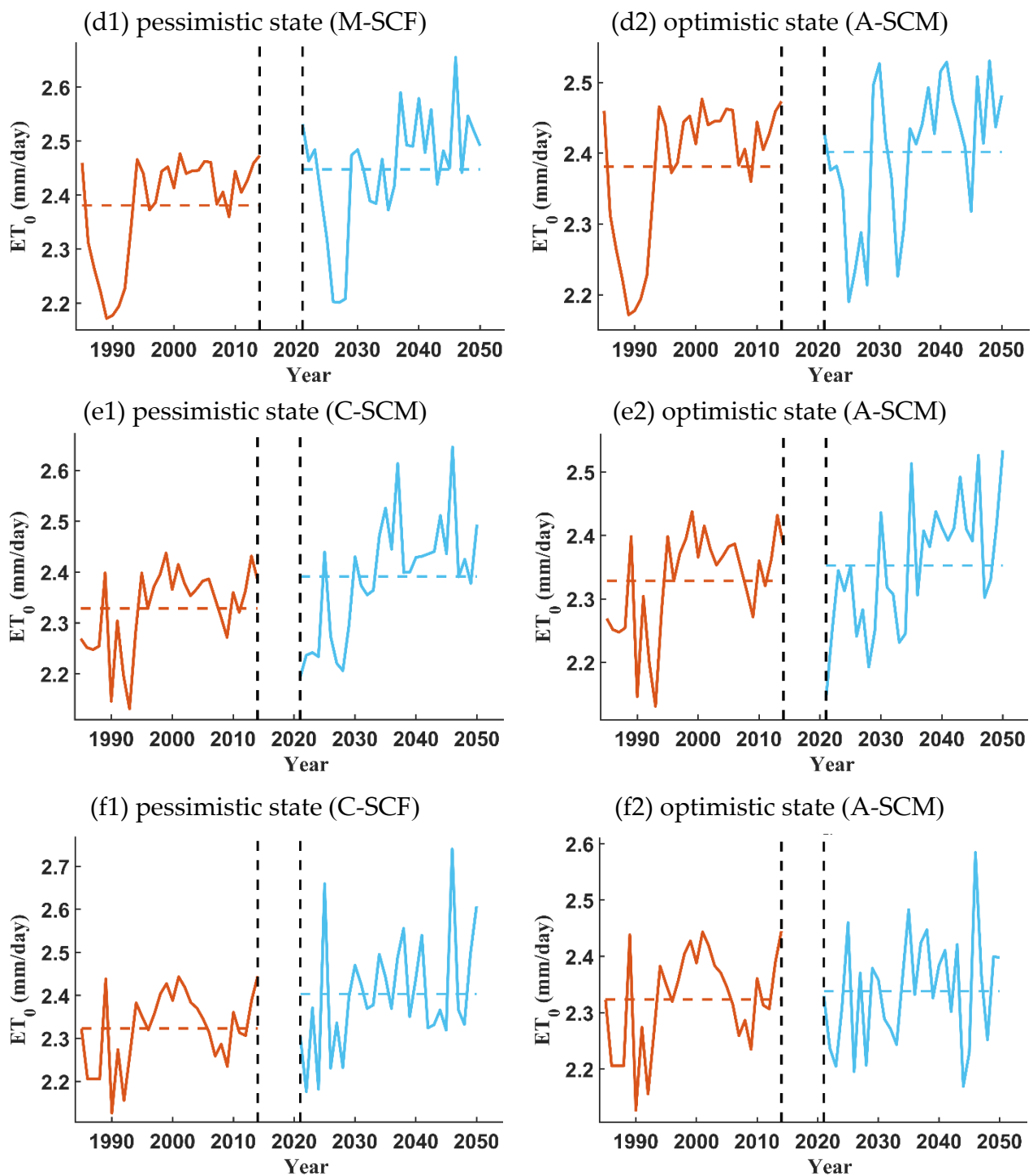


Figure A9. Cont.



**Figure A9.** Pessimistic and optimistic predictions of  $ET_0$  (a1,a2) Sahand, (b1,b2) Maragheh, (c1,c2) Mianeh, (d1,d2) Saqez, (e1,e2) Takab, (f1,f2) Zanja.

#### Appendix B.9

In Sahand station, the CanESM5 model and SCM scenario had less uncertainty (in this model and scenario, the amount of  $ET_0$  increased by 2.68%, which had less uncertainty than other models and scenarios). At Maragheh and Mianeh stations, the prediction of  $ET_0$  with the MRI-ESM2-0 model and SCS scenario was more probable (in this model and scenario, the amount of  $ET_0$  increased by 1.05%, and 1.84%, respectively, which had more certainty than other models and scenarios). In Saqez station, the predictions made by the CanESM5 model and SCM scenario had a high probability of occurrence (in this model

and scenario, the amount of ETo increased by 1.93%, which was more likely than in other models and scenarios). In the Takab station, the MRI-ESM2-0 model and SCF scenario had less uncertainty (in this model and scenario, the ETo value increased by 1.57%, which was more likely than in other models and scenarios). In the Zanjan station, the MRI-ESM2-0 model and SCS scenario had less uncertainty (in this model and scenario, the ETo value increased by 2.42%, which had less uncertainty than other models and scenarios).

Table A5. Results of uncertainty evaluation by MCM at the different stations.

	R-Factor								
	A-SCF	A-SCM	A-SCS	C-SCF	C-SCM	C-SCS	M-SCF	M-SCM	M-SCS
Sahand	2.452	2.442	2.450	2.451	2.396	2.430	2.422	2.426	2.419
Maragheh	2.774	2.768	2.767	2.763	2.760	2.761	2.752	2.748	2.747
Mianeh	2.012	2.005	1.995	2.013	1.991	1.992	1.986	1.990	1.979
Saqez	2.577	2.568	2.585	2.552	2.542	2.548	2.566	2.546	2.543
Takab	2.330	2.365	2.357	2.360	2.323	2.355	2.320	2.368	2.335
Zanjan	2.419	2.415	2.425	2.398	2.406	2.416	2.393	2.402	2.392

Appendix B.10

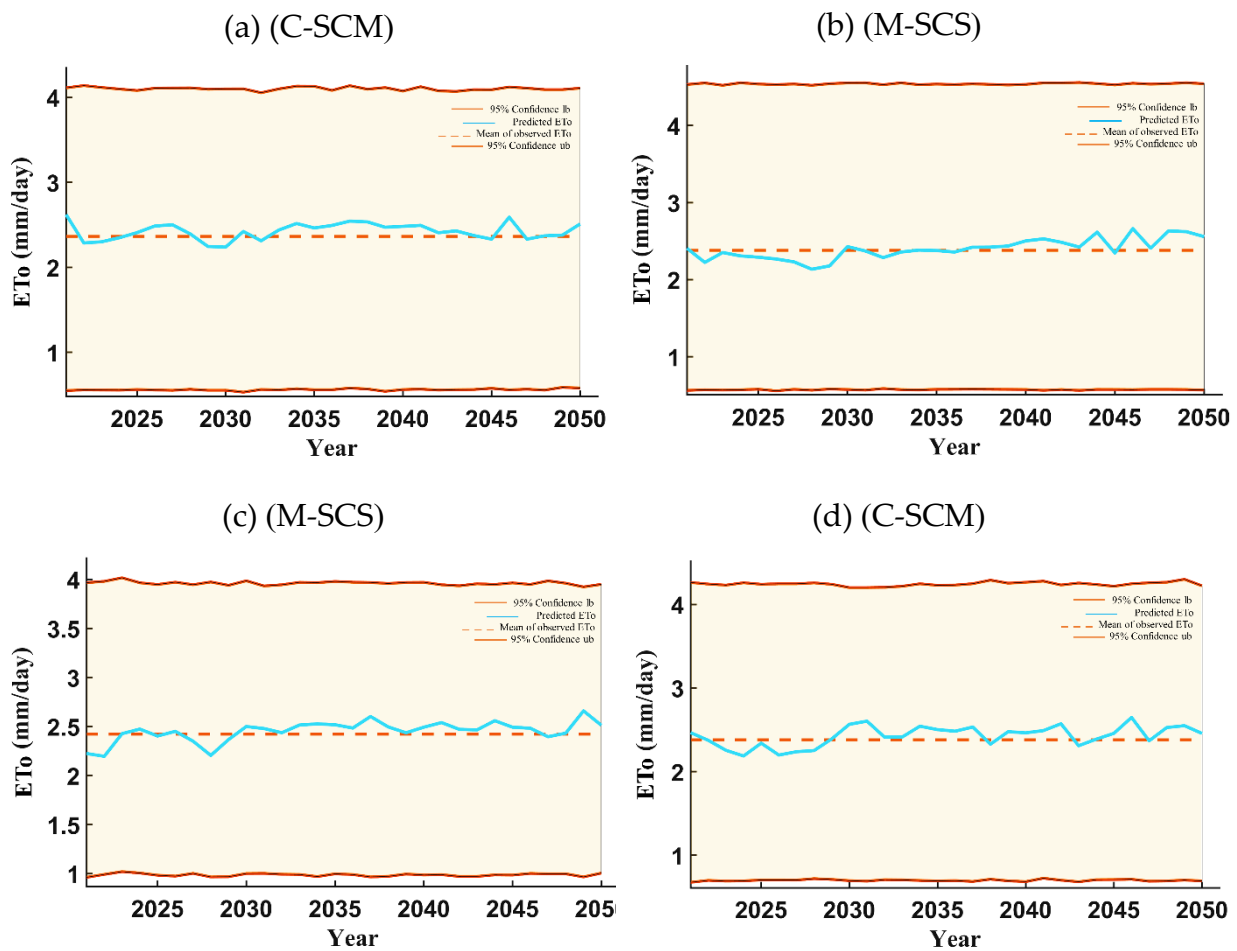
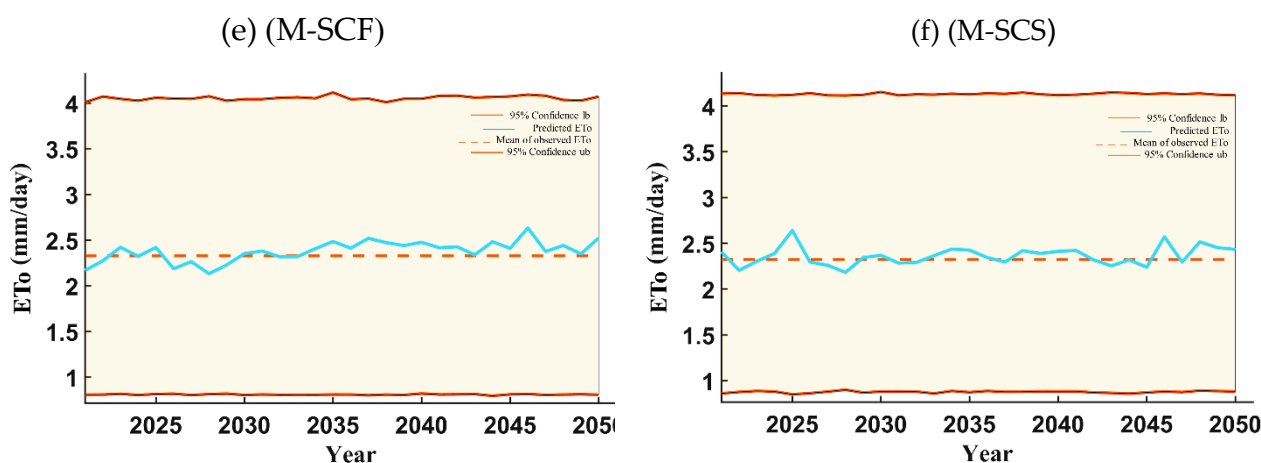


Figure A10. Cont.



**Figure A10.** The uncertainty bound for GCMs and scenarios with less uncertainty. (a) Sahand, (b) Maragheh, (c) Mianeh, (d) Saqez, (e) Takab, (f) Zanjan.

## References

- Wang, Z.; Zhan, C.; Ning, L.; Guo, H. Evaluation of global terrestrial evapotranspiration in CMIP6 models. *Theor. Appl. Climatol.* **2021**, *143*, 521–531. [[CrossRef](#)]
- Granata, F. Evapotranspiration evaluation models based on machine learning algorithms—A comparative study. *Agric. Water Manag.* **2019**, *217*, 303–315. [[CrossRef](#)]
- Sayyahi, F.; Farzin, S.; Karami, H. Forecasting Daily and Monthly Reference Evapotranspiration in the Aidoghmosh Basin Using Multilayer Perceptron Coupled with Water Wave Optimization. *Complexity* **2021**, *2021*, 6683759. [[CrossRef](#)]
- Allen, R.; Pereira, L.; Raes, D.; Smith, M.; Parte, C. *Crop Evapotranspiration (Guidelines for Computing Crop Water Requirements), Irrigation and Drainage Paper N 56*; Food and Agriculture Organization: Rome, Italy, 1998; Volume 300, p. D05109.
- Lama, G.F.C.; Rillo Migliorini Giovannini, M.; Errico, A.; Mirzaei, S.; Padulano, R.; Chirico, G.B.; Preti, F. Hydraulic Efficiency of Green-Blue Flood Control Scenarios for Vegetated Rivers: 1D and 2D Unsteady Simulations. *Water* **2021**, *13*, 2620. [[CrossRef](#)]
- Jones, C.D.; Hickman, J.E.; Rumbold, S.T.; Walton, J.; Lamboll, R.D.; Skeie, R.B.; Fiedler, S.; Forster, P.M.; Rogelj, J.; Abe, M.; et al. The Climate Response to Emissions Reductions Due to COVID-19: Initial Results from CovidMIP. *Geophys. Res. Lett.* **2021**, *48*, e2020GL091883. [[CrossRef](#)]
- Pachauri, R.K.; Reisinger, A. *Climate Change 2007: Synthesis Report. Contribution of Working Groups I, II and III to the Fourth Assessment Report of the Intergovernmental Panel on Climate Change*; IPCC: Geneva, Switzerland, 2007; pp. 1–104.
- Pachauri, R.K.; Meyer, L.A. *Climate Change 2014: Synthesis Report. Contribution of Working Groups I, II and III to the Fifth Assessment Report of the Intergovernmental Panel on Climate Change*; IPCC: Geneva, Switzerland, 2014; pp. 1–151.
- Eyring, V.; Bony, S.; Meehl, G.A.; Senior, C.A.; Stevens, B.; Stouffer, R.J.; Taylor, K.E. Overview of the Coupled Model Intercomparison Project Phase 6 (CMIP6) experimental design and organization. *Geosci. Model Dev.* **2016**, *9*, 1937–1958. [[CrossRef](#)]
- Su, B.; Huang, J.; Mondal, S.K.; Zhai, J.; Wang, Y.; Wen, S.; Gao, M.; Lv, Y.; Jiang, S.; Jiang, T.; et al. Insight from CMIP6 SSP-RCP scenarios for future drought characteristics in China. *Atmos. Res.* **2021**, *250*, 105375. [[CrossRef](#)]
- Monteiro, A.F.M.; Martins, F.B.; Torres, R.R.; Almeida, V.H.M.D.; Abreu, M.C.; Mattos, E.V. Intercomparison and uncertainty assessment of methods for estimating evapotranspiration using a high-resolution gridded weather dataset over Brazil. *Theor. Appl. Climatol.* **2021**, *146*, 583–597. [[CrossRef](#)]
- Muhammad, M.K.I.; Nashwan, M.S.; Shahid, S.; Ismail, T.b.; Song, Y.H.; Chung, E.S. Evaluation of Empirical Reference Evapotranspiration Models Using Compromise Programming: A Case Study of Peninsular Malaysia. *Sustainability* **2019**, *11*, 4267. [[CrossRef](#)]
- Allen, R.G.; Dhungel, R.; Dhungana, B.; Huntington, J.; Kilic, A.; Morton, C. Conditioning point and gridded weather data under aridity conditions for calculation of reference evapotranspiration. *Agric. Water Manag.* **2021**, *245*, 106531. [[CrossRef](#)]
- Ramírez-Cuesta, J.M.; Allen, R.G.; Intrigliolo, D.S.; Kilic, A.; Robison, C.W.; Trezza, R.; Santos, C.; Lorite, I.J. METRIC-GIS: An advanced energy balance model for computing crop evapotranspiration in a GIS environment. *Environ. Model. Softw.* **2020**, *131*, 104770. [[CrossRef](#)]
- Valikhan-Anaraki, M.; Mousavi, S.F.; Farzin, S.; Karami, H.; Ehteram, M.; Kisi, O.; Fai, C.M.; Hossain, M.S.; Hayder, G.; Ahmed, A.N.; et al. Development of a Novel Hybrid Optimization Algorithm for Minimizing Irrigation Deficiencies. *Sustainability* **2019**, *11*, 2337. [[CrossRef](#)]
- Yang, L.; Feng, Q.; Adamowski, J.F.; Yin, Z.; Wen, X.; Wu, M.; Jia, B.; Hao, Q. Spatio-temporal variation of reference evapotranspiration in northwest China based on CORDEX-EA. *Atmos. Res.* **2020**, *238*, 104868. [[CrossRef](#)]
- Ouhamdouch, S.; Bahir, M.; Ouazar, D.; Goumih, A.; Zouari, K. Assessment the climate change impact on the future evapotranspiration and flows from a semi-arid environment. *Arab. J. Geosci.* **2020**, *13*, 82. [[CrossRef](#)]

18. Tadese, M.; Kumar, L.; Koech, R. Long-Term Variability in Potential Evapotranspiration, Water Availability and Drought under Climate Change Scenarios in the Awash River Basin, Ethiopia. *Atmosphere* **2020**, *11*, 883. [[CrossRef](#)]
19. Niaghi, A.R.; Hassanijalilian, O.; Shiri, J. Estimation of Reference Evapotranspiration Using Spatial and Temporal Machine Learning Approaches. *Hydrology* **2021**, *8*, 25. [[CrossRef](#)]
20. Chia, M.Y.; Huang, Y.F.; Koo, C.H.; Fung, K.F. Recent Advances in Evapotranspiration Estimation Using Artificial Intelligence Approaches with a Focus on Hybridization Techniques—A Review. *Agronomy* **2020**, *10*, 101. [[CrossRef](#)]
21. Roy, D.K.; Lal, A.; Sarker, K.K.; Saha, K.K.; Datta, B. Optimization algorithms as training approaches for prediction of reference evapotranspiration using adaptive neuro fuzzy inference system. *Agric. Water Manag.* **2021**, *255*, 107003. [[CrossRef](#)]
22. Alizamir, M.; Kisi, O.; Adnan, R.M.; Kuriqi, A. Modelling reference evapotranspiration by combining neuro-fuzzy and evolutionary strategies. *Acta Geophys.* **2020**, *68*, 1113–1126. [[CrossRef](#)]
23. Sanikhani, H.; Kisi, O.; Maroufpoor, E.; Yaseen, Z.M. Temperature-based modeling of reference evapotranspiration using several artificial intelligence models: Application of different modeling scenarios. *Theor. Appl. Climatol.* **2019**, *135*, 449–462. [[CrossRef](#)]
24. Wu, L.; Peng, Y.; Fan, J.; Wang, Y. Machine learning models for the estimation of monthly mean daily reference evapotranspiration based on cross-station and synthetic data. *Hydrol. Res.* **2019**, *50*, 1730–1750. [[CrossRef](#)]
25. Ferreira, L.B.; da Cunha, F.F.; de Oliveira, R.A.; Filho, E.I.F. Estimation of reference evapotranspiration in Brazil with limited meteorological data using ANN and SVM—A new approach. *J. Hydrol.* **2019**, *572*, 556–570. [[CrossRef](#)]
26. Chen, H.; Huang, J.J.; McBean, E. Partitioning of daily evapotranspiration using a modified shuttleworth-wallace model, random forest and support vector regression, for a cabbage farmland. *Agric. Water Manag.* **2020**, *228*, 105923. [[CrossRef](#)]
27. Gocić, M.; Amiri, M.A. Reference Evapotranspiration Prediction Using Neural Networks and Optimum Time Lags. *Water Resour. Manag.* **2021**, *35*, 1913–1926. [[CrossRef](#)]
28. Gong, D.; Hao, W.; Gao, L.; Feng, Y.; Cui, N. Extreme learning machine for reference crop evapotranspiration estimation: Model optimization and spatiotemporal assessment across different climates in China. *Comput. Electron. Agric.* **2021**, *187*, 106294. [[CrossRef](#)]
29. Wu, L.; Fan, J. Comparison of neuron-based, kernel-based, tree-based and curve-based machine learning models for predicting daily reference evapotranspiration. *PLoS ONE* **2019**, *14*, e0217520. [[CrossRef](#)] [[PubMed](#)]
30. Walls, S.; Binns, A.D.; Levison, J.; MacRitchie, S. Prediction of actual evapotranspiration by artificial neural network models using data from a Bowen ratio energy balance station. *Neural Comput. Appl.* **2020**, *32*, 14001–14018. [[CrossRef](#)]
31. Kaya, Y.Z.; Zelenakova, M.; Unes, F.; Demirci, M.; Hlavata, H.; Mesáros, P. Estimation of daily evapotranspiration in Košice City (Slovakia) using several soft computing techniques. *Theor. Appl. Climatol.* **2021**, *144*, 287–298. [[CrossRef](#)]
32. Bellido-Jiménez, J.A.; Estévez, A.; García-Marín, A.P. New machine learning approaches to improve reference evapotranspiration estimates using intra-daily temperature-based variables in a semi-arid region of Spain. *Agric. Water Manag.* **2021**, *245*, 106558. [[CrossRef](#)]
33. Mohammadrezapour, O.; Piri, J.; Kisi, O. Comparison of SVM, ANFIS and GEP in modeling monthly potential evapotranspiration in an arid region (Case study: Sistan and Baluchestan Province, Iran). *Water Supply* **2019**, *19*, 392–403. [[CrossRef](#)]
34. Zhu, B.; Feng, Y.; Gong, D.; Jiang, S.; Zhao, L.; Cui, N. Hybrid particle swarm optimization with extreme learning machine for daily reference evapotranspiration prediction from limited climatic data. *Comput. Electron. Agric.* **2020**, *173*, 105430. [[CrossRef](#)]
35. Tikhamarine, Y.; Malik, A.; Souag-Gamane, D.; Kisi, O. Artificial intelligence models versus empirical equations for modeling monthly reference evapotranspiration. *Environ. Sci. Pollut. Res.* **2020**, *27*, 30001–30019. [[CrossRef](#)]
36. do Valle Júnior, L.C.G.; Vourlitis, G.L.; Curado, L.F.A.; da Silva Palácios, R.; de S. Nogueira, J.; de A. Lobo, F.; Islam, A.R.M.T.; Rodrigues, T.R. Evaluation of FAO-56 Procedures for Estimating Reference Evapotranspiration Using Missing Climatic Data for a Brazilian Tropical Savanna. *Water* **2021**, *13*, 1763. [[CrossRef](#)]
37. Rodrigues, G.C.; Braga, R.P. A Simple Procedure to Estimate Reference Evapotranspiration during the Irrigation Season in a Hot-Summer Mediterranean Climate. *Sustainability* **2021**, *13*, 349. [[CrossRef](#)]
38. Juneng, L.; Latif, M.T.; Tangang, F. Factors influencing the variations of PM10 aerosol dust in Klang Valley, Malaysia during the summer. *Atmos. Environ.* **2011**, *45*, 4370–4378. [[CrossRef](#)]
39. Huangfu, W.; Wu, W.; Zhou, X.; Lin, Z.; Zhang, G.; Chen, R.; Song, Y.; Lang, T.; Qin, Y.; Ou, P.; et al. Landslide Geo-Hazard Risk Mapping Using Logistic Regression Modeling in Guixi, Jiangxi, China. *Sustainability* **2021**, *13*, 4830. [[CrossRef](#)]
40. Adamowski, J.; Chan, H.F.; Prasher, S.O.; Ozga-Zielinski, B.; Sliusarieva, A. Comparison of multiple linear and nonlinear regression, autoregressive integrated moving average, artificial neural network, and wavelet artificial neural network methods for urban water demand forecasting in Montreal, Canada. *Water Resour. Res.* **2012**, *48*, W01528. [[CrossRef](#)]
41. Friedman, J.H. Multivariate Adaptive Regression Splines. *Ann. Stat.* **1991**, *19*, 1–67. [[CrossRef](#)]
42. Bozagaç, D.; Batmaz, I.; Oğuztüzün, H. Dynamic simulation metamodeling using MARS: A case of radar simulation. *Math. Comput. Simul.* **2016**, *124*, 69–86. [[CrossRef](#)]
43. Samadi, M.; Jabbari, E.; Azamathulla, H.M.; Mojallal, M. Estimation of scour depth below free overfall spillways using multivariate adaptive regression splines and artificial neural networks. *Eng. Appl. Comput. Fluid Mech.* **2015**, *9*, 291–300. [[CrossRef](#)]
44. Shan, X.; Cui, N.; Cai, H.; Hu, X.; Zhao, L. Estimation of summer maize evapotranspiration using MARS model in the semi-arid region of northwest China. *Comput. Electron. Agric.* **2020**, *174*, 105495. [[CrossRef](#)]
45. Quinlan, J.R.; Quinlan, J.R. Learning with Continuous Classes. In Proceedings of the 5th Australian Joint Conference on Artificial Intelligence, Hobart, Tasmania, 16–18 November 1992; World Scientific: Singapore, 1992; pp. 343–348.

46. Emamifar, S.; Rahimikhoob, A.; Noroozi, A.A. An Evaluation of M5 Model Tree vs. Artificial Neural Network for Estimating Mean Air Temperature as Based on Land Surface Temperature Data by MODIS-Terra Sensor. *Iran. J. Soil Water Res.* **2014**, *45*, 423–433. [[CrossRef](#)]
47. Bharti, B.; Pandey, A.; Tripathi, S.K.; Kumar, D. Modelling of runoff and sediment yield using ANN, LS-SVR, REPTree and M5 models. *Hydrol. Res.* **2017**, *48*, 1489–1507. [[CrossRef](#)]
48. Wang, Y.; Witten, I. *Induction of Model Trees for Predicting Continuous Classes*; University of Waikato: Hamilton, New Zealand, 1997.
49. Wang, Z.; Wang, Y.; Zeng, R.; Srinivasan, R.S.; Ahrentzen, S. Random Forest based hourly building energy prediction. *Energy Build.* **2018**, *171*, 11–25. [[CrossRef](#)]
50. Gholizadeh, M.; Jamei, M.; Ahmadianfar, I.; Pourrajab, R. Prediction of nanofluids viscosity using random forest (RF) approach. *Chemom. Intell. Lab. Syst.* **2020**, *201*, 104010. [[CrossRef](#)]
51. Breiman, L. Random Forests. *Mach. Learn.* **2001**, *45*, 5–32. [[CrossRef](#)]
52. Camacho-Navarro, J.; Ruiz, M.; Villamizar, R.; Mujica, L.; Moreno-Beltrán, G. Ensemble learning as approach for pipeline condition assessment. *J. Phys. Conf. Ser.* **2017**, *842*, 012019. [[CrossRef](#)]
53. Friedman, J.H. Greedy function approximation: A gradient boosting machine. *Ann. Statist.* **2001**, *29*, 1189–1232. [[CrossRef](#)]
54. Yoon, K.P.; Hwang, C.L. Multiple Attribute Decision Making: An Introduction. In *Quantitative Applications in the Social Sciences*, 1st ed.; Sage Publications Inc.: Thousand Oaks, CA, USA, 1995; Volume 104, pp. 1–83. [[CrossRef](#)]
55. Farzin, S.; Anaraki, M.V. Modeling and predicting suspended sediment load under climate change conditions: A new hybridization strategy. *J. Water Clim. Chang.* **2021**, *12*, 2422–2443. [[CrossRef](#)]
56. Anandhi, A.; Frei, A.; Pierson, D.C.; Schneiderman, E.M.; Zion, M.S.; Lounsbury, D.; Matonse, A.H. Examination of change factor methodologies for climate change impact assessment. *Water Resour. Res.* **2011**, *47*, W03501. [[CrossRef](#)]
57. Diaz-Nieto, J.; Wilby, R.L. A comparison of statistical downscaling and climate change factor methods: Impacts on low flows in the River Thames, United Kingdom. *Clim. Chang.* **2005**, *69*, 245–268. [[CrossRef](#)]
58. Anaraki, M.V.; Farzin, S.; Mousavi, S.F.; Karami, H. Uncertainty Analysis of Climate Change Impacts on Flood Frequency by Using Hybrid Machine Learning Methods. *Water Resour. Manag.* **2020**, *35*, 199–223. [[CrossRef](#)]
59. Asadollah, S.B.H.S.; Sharafati, A.; Motta, D.; Yaseen, Z.M. River water quality index prediction and uncertainty analysis: A comparative study of machine learning models. *J. Environ. Chem. Eng.* **2021**, *9*, 104599. [[CrossRef](#)]
60. Farrokhi, A.; Farzin, S.; Mousavi, S.F. A new framework for evaluation of rainfall temporal variability through principal component analysis, hybrid adaptive neuro-fuzzy inference system, and innovative trend analysis methodology. *Water Resour. Manag.* **2020**, *34*, 3363–3385. [[CrossRef](#)]
61. Farzin, S.; Chianeh, F.N.; Anaraki, M.V.; Mahmoudian, F. Introducing a framework for modeling of drug electrochemical removal from wastewater based on data mining algorithms, scatter interpolation method, and multi criteria decision analysis (DID). *J. Clean. Prod.* **2020**, *266*, 122075. [[CrossRef](#)]
62. Kadkhodazadeh, M.; Farzin, S. A Novel LSSVM Model Integrated with GBO Algorithm to Assessment of Water Quality Parameters. *Water Resour. Manag.* **2021**, *35*, 3939–3968. [[CrossRef](#)]
63. Hamidi, S.M.; Fürst, C.; Nazmfar, H.; Rezayan, A.; Yazdani, M.H. A Future Study of an Environment Driving Force (EDR): The Impacts of Urmia Lake Water-Level Fluctuations on Human Settlements. *Sustainability* **2021**, *13*, 11495. [[CrossRef](#)]
64. Forster, P.M.; Forster, H.I.; Evans, M.J.; Gidden, M.J.; Jones, C.D.; Keller, C.A.; Lamboll, R.D.; Quéré, C.L.; Rogelj, J.; Rosen, D.; et al. Current and future global climate impacts resulting from COVID-19. *Nat. Clim. Chang.* **2020**, *10*, 913–919. [[CrossRef](#)]
65. Lamboll, R.D.; Jones, C.D.; Skeie, R.B.; Fiedler, S.; Samset, B.H.; Gillett, N.P.; Rogelj, J.; Forster, P.M. Modifying emissions scenario projections to account for the effects of COVID-19: Protocol for CovidMIP. *Geosci. Model Dev.* **2021**, *14*, 3683–3695. [[CrossRef](#)]
66. D'Souza, J.; Valayannopoulos-Akrivou, L.; Sherman, P.; Penn, E.; Song, S.; Archibald, A.T.; McElroy, M.B. Projected changes in seasonal and extreme summertime temperature and precipitation in India in response to COVID-19 recovery emissions scenarios. *Environ. Res. Lett.* **2021**, *16*, 114025. [[CrossRef](#)]
67. Farrokhi, A.; Farzin, S.; Mousavi, S.F. Meteorological drought analysis in response to climate change conditions, based on combined four-dimensional vine copulas and data mining (VC-DM). *J. Hydrol.* **2021**, *603*, 127135. [[CrossRef](#)]
68. Riahi, K.; van Vuuren, D.P.; Kriegler, E.; Edmonds, J.; O'Neill, B.C.; Fujimori, S.; Bauer, N.; Calvin, K.; Dellink, R.; Fricko, O.; et al. The Shared Socioeconomic Pathways and their energy, land use, and greenhouse gas emissions implications: An overview. *Glob. Environ. Chang.* **2017**, *42*, 153–168. [[CrossRef](#)]
69. Ziehn, T.; Chamberlain, M.A.; Law, R.M.; Lenton, A.; Bodman, R.W.; Dix, M.; Stevens, L.; Wang, Y.P.; Sribnovsky, J. The Australian Earth System Model: ACCESS-ESM1.5. *J. South. Hemisph. Earth Syst. Sci.* **2020**, *70*, 193–214. [[CrossRef](#)]
70. Swart, N.C.; Cole, J.N.S.; Khari, V.V.; Lazare, M.; Scinocca, J.F.; Gillett, N.P.; Anstey, J.; Arora, V.; Christian, J.R.; Hanna, S.; et al. The Canadian Earth System Model version 5 (CanESM5.0.3). *Geosci. Model Dev.* **2019**, *12*, 4823–4873. [[CrossRef](#)]
71. Yukimoto, S.; Kawai, H.; Koshiro, T.; Oshima, N.; Yoshida, K.; Urakawa, S.; Tsujino, H.; Deushi, M.; Tanaka, T.; Hosaka, M.; et al. The Meteorological Research Institute Earth System Model Version 2.0, MRI-ESM2.0: Description and Basic Evaluation of the Physical Component. *J. Meteorol. Soc. Jpn.* **2019**, *97*, 931–965. [[CrossRef](#)]
72. Oshima, N.; Yukimoto, S.; Deushi, M.; Koshiro, T.; Kawai, H.; Tanaka, T.Y.; Yoshida, K. Global and Arctic effective radiative forcing of anthropogenic gases and aerosols in MRI-ESM2.0. *Prog. Earth Planet. Sci.* **2020**, *7*, 38. [[CrossRef](#)]